BENEMÉRITA UNIVERSIDAD AUTÓNOMA DE PUEBLA

INSTITUTO DE FÍSICA “LUIS RIVERA TERRAZAS”

“SPECTRAL DESIGN OF METAMATERIALS WITH NON-ORTHOGONAL ORBITALS”

THESIS

MASTER OF SCIENCE
(PHYSICS)

PRESENTED BY
JOSE GUADALUPE SANTIAGO GARCIA

SUPERVISOR
DR. EMERSON LEAO SADURNÍ HERNÁNDEZ

CVU Number: 1147151

OCTOBER 2023

Benemérita Universidad Autónoma de Puebla
Instituto de Física "Luis Rivera Terrazas"

Spectral design of metamaterials with non-orthogonal orbitals

A thesis presented by

JOSE GUADALUPE SANTIAGO GARCIA

to attain the degree of

Master of Science
(Physics)

Supervisor
DR. EMERSON LEAO SADURNÍ HERNÁNDEZ

Puebla, México
October 2023

Agradecimientos

Gracias a todos los que han hecho posible la realización de mis estudios de maestría. Agradezco a mi asesor de tesis, el Dr. Emerson Sadurní, por su constante guía y enseñanza y a mi comité tutorial por el tiempo destinado para la revisión de esta tesis. También agradezco a amigos y profesores por todo lo que he aprendido de ellos. Gracias a la familia De los Santos Gómez por toda la ayuda brindada durante la etapa de actividades presenciales. Finalmente, agradezco a mi familia por su invaluable apoyo en todo momento.

JOSE GUADALUPE SANTIAGO GARCIA

Puebla, México

Octubre, 2023

Dedico este trabajo a mi familia

Diseño espectral de metamateriales con orbitales no ortogonales

Resumen

Considerando traslapes entre estados atómicos aislados que son vecinos más cercanos, se logra una descripción de espectros deformados para sistemas que van desde una configuración dimérica de pozos de potencial hasta configuraciones aperiódicas con espectros específicos, pasando por arreglos traslacionalmente invariantes. Para el primer sistema, se hace una comparación entre las predicciones de un modelo de amarre fuerte con orbitales no ortogonales y el espectro experimental de un par de discos cerámicos, logrando describir correctamente el fenómeno de la separación asimétrica de los niveles de energía. Las funciones de Wannier se investigan en este contexto y se calculan tanto para el caso dímerico como para el periódico. La libertad de fase en el ajuste de la localización de estas últimas funciones se ilustra con un par de ejemplos. Una ecuación secular para el espectro deformado de un conjunto compacto de pozos de potencial permite el diseño de eigenvalores de energía aproximadamente equiespaciados. Finalmente, se introduce un método numérico para el estudio de propiedades de transporte de potenciales unidimensionales con punto de referencia recorrido. Estas consideraciones pueden ser relevantes en la miniaturización de cristales artificiales así como en la fabricación de un dispositivo electrónico isócrono, cuya frecuencia de oscilación se estima mayor que la de los osciladores de cuarzo actuales.

Spectral design of metamaterials with non-orthogonal orbitals

Abstract

By considering overlaps between nearest-neighbor isolated atomic states, a description of deformed spectra is achieved for systems that range from a dimeric configuration of potential wells up to aperiodic structures with specific spectra, passing through translationally invariant arrays. For the first system, a comparison is made between predictions from a tight-binding model with non-orthogonal orbitals and the experimental spectrum of a pair of ceramic disks, succeeding in correctly describing the phenomenon of asymmetric splitting of energy levels. Wannier functions are investigated in this context and are calculated for both the dimeric and periodic cases. The freedom of phase for localization adjustment of the latter functions is illustrated with a pair of examples. A secular equation for the deformed spectrum of a compact set of potential wells enables the engineering of nearly equispaced energy eigenvalues. Then, the concept of an all-electronic clock is briefly discussed and the coherent evolution of wavepackets is presented for a particular aperiodic configuration. Finally, a numerical method for the study of transport properties of one-dimensional shifted potentials is introduced. These considerations may be relevant in the miniaturization of artificial crystals as well as in the fabrication of an isochronous electronic device which is estimated to work at higher frequencies than current quartz oscillators.

Participation in events

- *Non-orthogonal orbitals for the double square well potential*, J. G. SANTIAGO GARCIA, E. Sadurní, Wave dynamics in complex systems and more, International Center of Sciences, Cuernavaca, Morelos, México (2022).
- *Funciones de Wannier para cadenas con orbitales traslapantes*, J. G. SANTIAGO GARCIA, E. Sadurní, Simposio Estudiantil del Posgrado en Física IFUAP 2023, Puebla, Puebla, México (2023).

Table of contents

List of Figures

List of Tables

Chapter 1

Introduction

1.1 Metamaterials and spectral emulations

Metamaterials are physical systems that display properties which are artificially produced. Important examples are found in [1–3]. One way of obtaining extraordinary properties is through the modification of the energy or frequency spectrum for waves that propagate within such class of media. A similar task is carried out in the field of mesoscopic spectral emulations, which are a way of studying, in an experimental setting, fundamental models in analog systems that, otherwise, would be difficult to manipulate or control. The aim of the emulations is to reproduce models of interest on analog platforms whose dimensions (size) are on the mesoscopic scale, giving rise to the possibility of flexibly and precisely adjusting the geometric control parameters. For example, the successful emulation of a Dirac oscillator was reported in [4], while other relativistic and finite models such as the Dirac gyroscope were studied in [5], making it possible to implement them with the help of ceramic disks [6].

On the other hand, on microscopic scales, crystalline systems offer technical and financial challenges regarding the geometric manipulation necessary to modulate their electronic and phononic transport properties; a relevant example on this scale was reported in [7]. The study of graphene, both experimentally [8] and theoretically [9, 10], constitutes a paradigmatic example in which lattice deformations play an important role. The wave transmission properties, including the electronic case, suffer the effect of such deformations in artificial realizations reported in [11–22]. Furthermore, some types of mechanical stress of the material can be emulated in this type of implementation [23, 24]. It is worth mention-

ing that the so-called Dirac points have been observed in artificial crystals as well, with or without deformation [25]. Clearly, these investigations have led to a renewed interest in the close study of tight-binding chains [26], where the non-orthogonality of localized orbitals may play an important role.

1.2 Motivation to study tight-binding models with non-orthogonal orbitals

In the nearest neighbor approximation of tight-binding models it is usually assumed that the states located at the lattice sites are such that the inner product between adjacent wavefunctions is zero. However, the predicted energy levels at the edges of the bands show slight deviations between the model and the experiment [6,18], making clear the need for non-orthogonal orbitals. In Refs. [17,27], it was shown that when the usual regime of dilute arrays of potential wells is not fulfilled, the spectrum of a finite oscillator begins to deform. Second neighbor contributions have been put forward as a possible explanation of such a behavior. On the other hand, the experimental spectrum of a pair of ceramic disks [18] constitutes an ideal setting where the second neighbor contribution idea can be tested. In Ref. [18] the spectral asymmetry of such type of dimer is exposed. Such result points to the introduction of overlapping localized states as responsible for the deformation. All of these observations have given place to the present work, leading us to consider the corresponding corrections, including the calculation of the Wannier functions for the systems under scrutiny. We call our engineered arrays of potential wells metamaterials because their resulting energy spectra come from the designed lattice geometry. Furthermore, the individual constituents of the diverse physical realizations of our tight-binding models, such as quantum dots, microwave billiards, optical lattices, phononic and photonic crystals, do not posses the energy or frequency spectrum of the system as a whole.

1.3 Objectives and outline of this work

1.3.1 General objective

- The general objective of this work is to develop tight-binding models with non-orthogonal orbitals for geometrically deformed metamaterials.

1.3.2 Particular objectives

Our particular objectives are:

- To emulate the asymmetric resonance of ceramic disks with two potential wells in one dimension, with analytical solutions and with non-orthogonal bases and to verify the phenomenon of resonance asymmetry or deformed spectrum.
- To find frequency bands with electron-hole asymmetry (deformed valence-conduction band) in chains of potential wells and their electromagnetic counterpart made with ceramics.
- To use non-orthogonal orbitals to correct the Wannier transform.
- To look for aperiodic and compact configurations of potential wells (e. g. finite oscillator) that posses energy spectra corrected by non-orthogonal localized bases.

This thesis is structured as follows: In chapter two, the emulation of the deformed spectrum of a pair of dielectric disks is presented. The asymmetric splitting of energy levels in a dimeric quantum system is reviewed and a tight-binding Hamiltonian, written in a non-orthogonal basis of localized states, is diagonalized with the help of the matrix of inner products. The resulting analytical expressions for energy eigenvalues are then adjusted to available experimental data by means of an effective Schrödinger equation for electromagnetic waves in cavities. In the third chapter, our efforts are devoted to extend the formalism, introduced for a dimer, to infinite chains of evenly spaced lattice sites. Results from this task are compared with the exact Kronig-Penney solution in a regime of densely placed potential wells, in which case deformed bands are found. Chapter four contains some results regarding the estimation of Wannier functions when localized atomic orbitals overlap. Continuing, chapter 5 presents the study of a generalized eigenvalue equation for the asymmetric spectrum of compactly distributed lattice sites. Said study makes possible the engineering of specific spectra, in particular, an equispaced one. The latter spectrum gives place to the idea of an isocrhonous device working with electronic wavepackets, which is briefly discussed in the same chapter. Lastly, the calculation of the resonance spectrum of lifted finite chains of potential wells is introduced in chapter 6. Conclusions are given in chapter 7.

Chapter 2

Emulating the deformed spectrum of a dimer

In this chapter, the deformed spectrum of a pair of dielectric disks is emulated using a non-orthogonal basis of localized states. We start this chapter by presenting a result regarding energy level asymmetric splitting for a dimer and then we proceed to explain in detail all the necessary considerations in the description. We do so progressively by first reviewing the absence of symmetry in the separation of the two lowest energy levels of dimeric quantum systems as a function of a parameter, e.g. the separation between compartments or the intensity of a potential barrier. Then, we pose the problem of a system of two wells with non-negligible nearest-neighbor overlap as a tight-binding model with a non-orthogonal basis and solve for the spectrum. It is found that energy levels split asymmetrically as a function of distance between wells, thus explaining the origin of the deformation. Lastly, it is explained how analytical expressions were adjusted to available experimental data. In all, a good agreement between theory and experiment has been found.

2.1 Experimental data and presentation of results

In the left panel of Fig. 2.1 the experimental transmission spectrum of a pair of ceramic disks between two conductive plates [18] is shown. The intensity peaks correspond to the system's transmission understood as $1 - |R|^2$, where $|R|^2$ is the measured reflection power. One can see that frequencies unfold asymmetrically from the mean, something that cannot be described by a simple tight-binding model with orthogonal localized states of a

single potential well. By looking carefully at the region of distances between disks, which have a diameter $D = 8$mm, close to 1mm, one can note the asymmetry between even states (bright yellow points of frequency 6.58GHz) and odd states (purple points of frequency 6.81GHz) with respect to the degenerate isolated resonance at 6.66GHz. Each cylinder in the right panel of Fig. 2.1 supports a bound state.

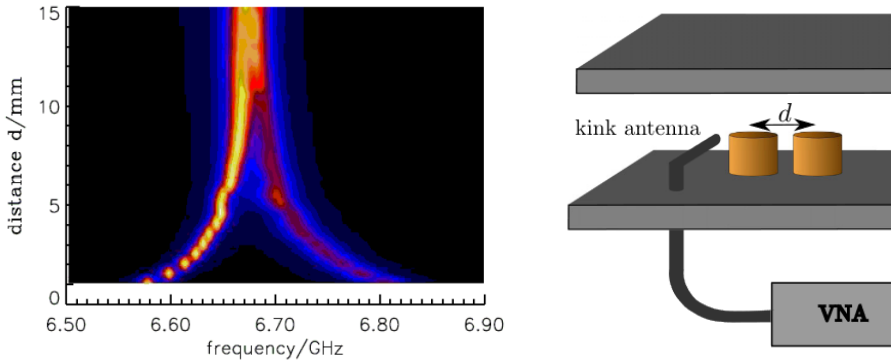

Figure 2.1: Left: Density plot of the transmission coefficient (yellow maximum, black minimum) of a pair of ceramic cylinders placed between two conductive plates [18]. The individual resonance, $\omega = 6.66$ GHz, is recovered at large separation distances. The eigenfrequencies split asymmetrically as the distance between disks diminishes. Right: In the experiment, the reflection is measured by placing a transmitter antenna on a disk and detecting with the same antenna, connected to a vector network analyzer (VNA).

The origin of the spectral deformation is identified as the outcome of non-negligible overlaps between contiguous isolated states. To show that this is indeed the case, we have calculated the energy levels of a dimer with a tight-binding model using a basis of non-orthogonal atomic states. In microwave billiards [29], the aforementioned basis consists of isolated bound states in each cylindrical resonator. The dot product of these vectors does not vanish, although it is considered small indeed. In fact, the projection of one vector with its neighbor is of the order of 1/10, when normalized to the total energy. For the relevant field component E_z, we have

$$\int |E_z|^2 dV = \text{Energy}, \quad E_z = E_0 \psi(x,y)\cos(kz), \quad \int |\psi|^2 \, dA = 1, \tag{2.1}$$

where dV is the volume element and dA is the area element of the plane perpendicular to the field, in this case the xy-plane. Then, our statement about the overlap parameter

translates into

$$\int \psi_1{}^* \psi_2 \, dA \sim 10^{-1}. \tag{2.2}$$

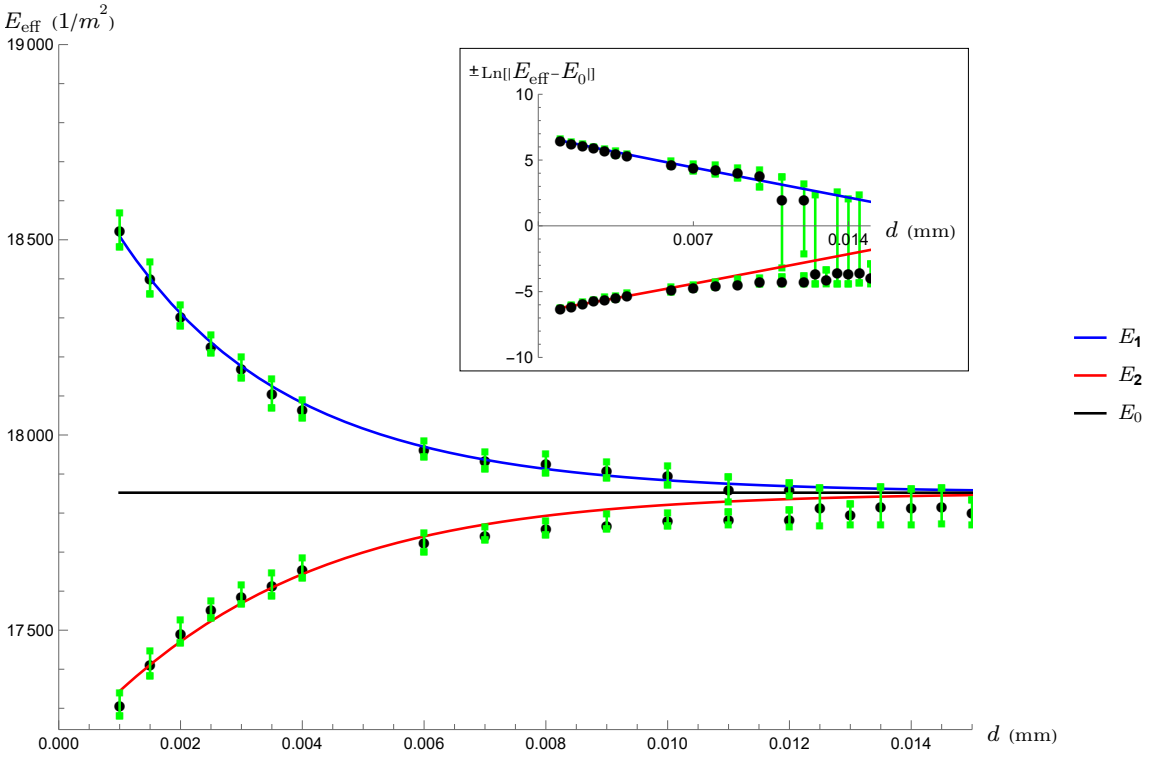

Figure 2.2: Spectral emulation with non-orthogonal orbitals. Comparison between the theoretical (solid lines) and experimental (black points with green uncertainty bars) spectrum. An spectral asymmetry for a pair of ceramic disks in the microwave region is visible in effective energy variables, E_{eff}, Eq. (2.22). The inset shows a semi-log plot of the emulation.

Figure 2.2 depicts, with solid lines, the behavior of the resulting energy eigenvalues as a function of the distance between disks, which is measured from the edges of the potential wells. The theoretical model, which is fully explained in section 2.3, is contrasted against the experimental data read from Fig 2.1. In making this comparison, experimental frequency variables have been mapped to effective energy variables by means of an analogous Schrödinger equation obtained from the Helmholtz wave equation, i.e. Energy $=$ (Frequency$/c)^2$, provided $\hbar^2/2m = 1$. This last point is further explained in the last section of this chapter. The theoretical values thus obtained coincide satisfactorily with the experimental spectrum of a pair of dielectric disks, as can be seen from the ac-

companying green bars which represent the uncertainty in the value of the measured power. This shows that our starting assumption about overlaps between neighboring bound states as responsible for the spectral asymmetry is true. In order to explain the physical conditions that make this emulation possible, we first review the behavior of energy levels of dimeric quantum systems in one dimension, looking for deformations. Then, the use of a non-orthogonal basis is explained. Finally, the quantum-to-electromagnetic analogy is established.

2.2 Review of asymmetrical splitting in dimers

The following problems illustrate the inherent spectral asymmetry of dimeric quantum systems. The treatment presented here is original albeit based on standard techniques of smooth matching across boundaries.

2.2.1 Two wells: graphical method

The quantum mechanical problem, in units where $\hbar^2/2m = 1$, defined by the specification of the following potential function

$$V(x) = \begin{cases} 0, & \text{for } a < |x| < a + L, \\ V_0, & \text{for } |x| < a, \\ \infty, & \text{for } |x| > a + L, \end{cases} \tag{2.3}$$

for the stationary Schrödinger equation,

$$-\frac{d^2\psi}{dx^2} + V(x)\psi = E\psi, \tag{2.4}$$

has odd and even solutions, see the left panel of Fig. 2.3.

Energies are determined from trascendental equations, whose mathematical expression depend on whether the wavefunction is even or odd. We have

$$-\frac{\tan\left(\sqrt{\epsilon}\tilde{L}\right)}{\sqrt{\epsilon}} = \begin{cases} \dfrac{\coth\left(\sqrt{(\epsilon-1)}\tilde{a}\right)}{\sqrt{(\epsilon-1)}} & \text{even}, \\ \dfrac{\tanh\left(\sqrt{(\epsilon-1)}\tilde{a}\right)}{\sqrt{(\epsilon-1)}} & \text{odd}. \end{cases} \tag{2.5}$$

In the previous equation $\epsilon = E/V_0$, $\tilde{L} = L\sqrt{V_0}$ and $\tilde{a} = a\sqrt{V_0}$ are all dimensionless variables. If one wishes to recover the original units, it is enough to substitute $\sqrt{V_0} \to \sqrt{2mV_0/\hbar^2}$.

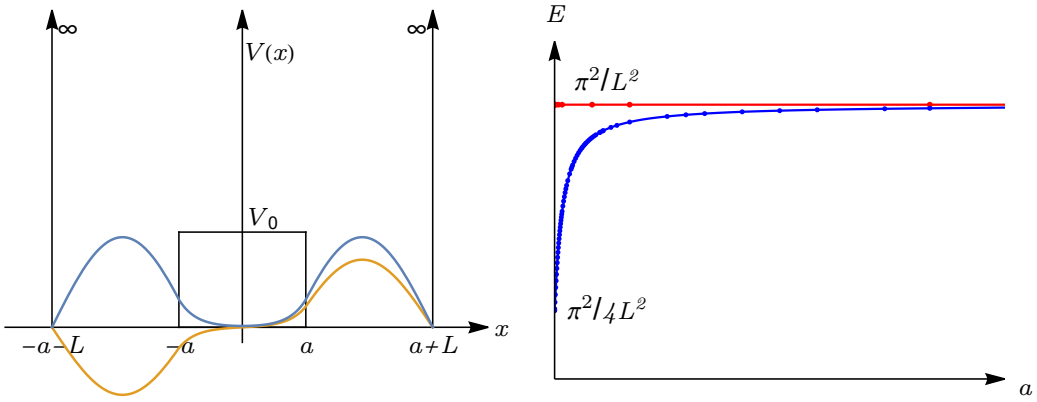

Figure 2.3: Left panel: Double square well potential with the lowest energy eigenstates superimposed. Right panel: Energies of the lowest states for the double square well as a function of the distance between wells. $V_0 = 100 \times [\hbar^2/2mL^2]$.

The energies of the two lowest eigenstates of this system, called the symmetric and antisymmetric states, with energies E_S and E_A, respectively, behave as depicted in the right panel of Fig. 2.3, when the separation between wells is varied. This figure makes evident the asymmetrical splitting of these energy levels.

2.2.2 Infinite well plus delta barrier

As another example of the family of quantum mechanical problems that displays the phenomenon of asymmetric level splitting, let us consider

$$V(x) = \begin{cases} \infty & \text{for } |x| \geq l/2, \\ -\gamma\delta(x) & \text{for } |x| < l/2. \end{cases} \tag{2.6}$$

i.e., the infinite square well with a delta obstacle at its center. Odd, or antisymmetric, states have $k_{\text{odd}} = 2n\pi/l$, $n \in \mathbb{N}$, and even, or symmetric states, can be studied by setting $E = -k^2$, as it turns out that they can have both negative ($k \in \mathbb{R}\backslash\{0\}$) or positive energies ($k \to ik$, k$\in \mathbb{R}\backslash\{0\}$)[1]. For $E < 0$, the corresponding wave functions are encoded in the

[1]The case $k = 0$ makes the wavefunction vanish trivially and thus it is dropped from our considerations.

following expression:

$$\psi(x) = \mathcal{N}(e^{kl/2}e^{-k|x|} - e^{-kl/2}e^{k|x|}), \tag{2.7}$$

where $\mathcal{N} = \sqrt{k/\{2\,[\sinh(kl) - kl]\}}$. To determine the allowed k values, the corresponding trascendental equation found in Table 2.1, has to be solved graphically. If $\gamma < 0$, then there are no bound states with negative energies and the only solution, which is $k = 0$, is forbidden. All cases, including the remaining for $E > 0$, have been succinctly summarized in Table 2.1.

Table 2.1: Classification of even eigenstates for the potential given by Eq. (2.6) according to their energies and sign of γ (attractive or repulsive potential). The corresponding trascendental equation is shown, $k \in \mathbb{R}\backslash\{0\}$, $\hbar^2/2m = 1$, $\gamma \neq 0$.

Classification of even eigenstates for potential and the corresponding trascendental equation		
	ATTRACTIVE	REPULSIVE
	$\gamma > 4/l$	$\gamma < 0$
$E < 0$	✓ $k = \frac{\lvert\gamma\rvert}{2}\tanh(kl/2)$	✗ –
	$\gamma > 0$	$\gamma < 0$
$E > 0$	✓ $k = \frac{\lvert\gamma\rvert}{2}\tan(kl/2)$	✓ $k = -\frac{\lvert\gamma\rvert}{2}\tan(kl/2)$

In appendix A the details are given regarding the derivation of Eq. (2.7) as a solution of the stationary Schrödinger equation for the potential given by Eq. (2.6) and $E = -k^2$. In Fig. 2.4, representative wavefunctions have been drawn inside the potential well. Fig. 2.5 shows the asymmetric splitting of the lowest energy levels of this problem.

From these exactly solvable problems we can appreciate that energy levels unfold asymmetrically for small values of the corresponding relevant parameter, thus finding the spectral asymmetry to be an inherent phenomenon of a dimeric quantum system with strong coupling. In the next section, we are going to obtain the explicit expressions for the energies of a dimer from a tight-binding model with a non-orthogonal basis, giving place to yet another deformed dimeric spectrum.

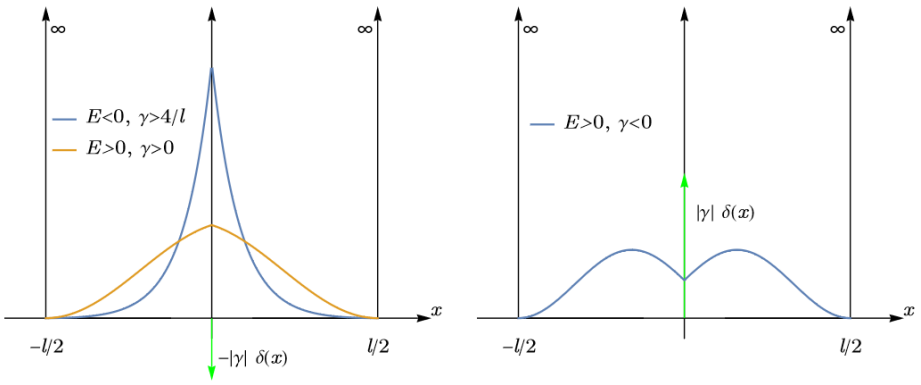

Figure 2.4: Ground state probability distributions according to the sign of γ and the energy of the wave. Left panel: attractive delta; both positive and negative bound state energies are allowed. Right panel: repulsive potential inside the box. The green arrow represents the sign of the potential.

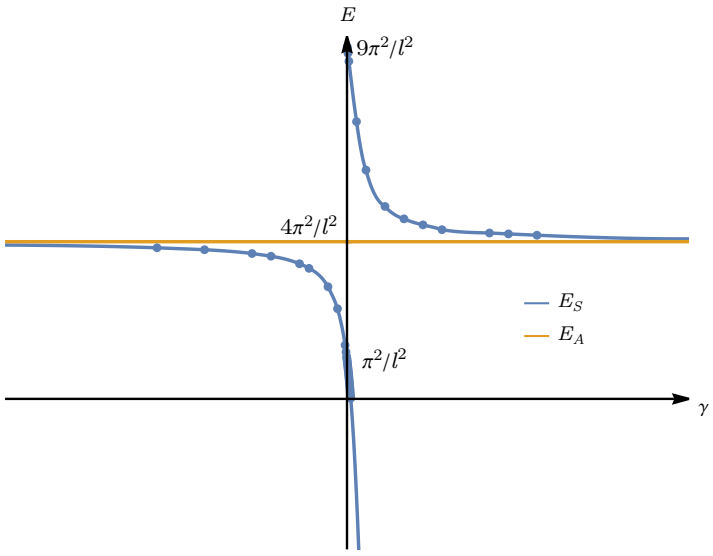

Figure 2.5: Lowest energy levels as a function of γ. Negative (positive) values correspond to a repulsive (attractive) potential.

2.3 Tight-binding model with non-neglible nearest-neighbor overlaps

Here it is shown that, by considering a non-orthogonal basis of localized states, one can describe the spectral deformation of a pair of potential wells. The proposed formalism will enable us to explore other systems beyond the double square well problem.

In the tight-binding approximation we take localized states (atomic orbitals), denoted by $|n\rangle$, as our Wannier functions, which obey $\langle n|m\rangle = \delta_{nm}$. Now, we will work under the assumption of overlapping of atomic orbitals, namely

$$\langle n|m\rangle \neq \delta_{nm}, \tag{2.8}$$

so that this time we do not know the Wannier functions of the system. For a dimer, we are interested in the non-orthogonal basis $\{|1\rangle, |2\rangle\}$ such that

$$\langle 1|1\rangle = \langle 2|2\rangle = 1, \qquad 1 > \langle 1|2\rangle = \langle 2|1\rangle = \epsilon > 0. \tag{2.9}$$

We want to find the spectrum and eigenstates of a tight-binding Hamiltonian which, in the basis just introduced, is written as

$$H = E_0(|1\rangle\langle 1| + |2\rangle\langle 2|) - \Delta(|1\rangle\langle 2| + |2\rangle\langle 1|). \tag{2.10}$$

It is important to note that Δ and E_0 are tight-binding parameters, but they can be defined in terms of overlap integrals of the Hamiltonian. In Eqs. (2.25) and (2.26) both Δ and ϵ are expressed as functions of the distance between wells. Given the nature of this basis, we cannot use it to write the matrix representation of the Hamiltonian operator directly. However, we can make a change of basis such that it diagonalizes the hermitian operator H, leading automatically to orthogonality. To do this let us consider the inner product matrix

$$D := \begin{pmatrix} \langle 1|1\rangle & \langle 1|2\rangle \\ \langle 2|1\rangle & \langle 2|2\rangle \end{pmatrix} = \begin{pmatrix} 1 & \epsilon \\ \epsilon & 1 \end{pmatrix} \tag{2.11}$$

which is diagonalized to $\tilde{D}$, given by

$$\tilde{D} = \begin{pmatrix} 1-\epsilon & 0 \\ 0 & 1+\epsilon \end{pmatrix} =: \begin{pmatrix} (1|1) & (1|2) \\ (2|1) & (2|2) \end{pmatrix} \tag{2.12}$$

through a similarity transformation that employs the matrix

$$P = \frac{1}{\sqrt{2}} \begin{pmatrix} 1 & 1 \\ -1 & 1 \end{pmatrix} \tag{2.13}$$

with inverse $P^{-1} = P^T$, such that $\tilde{D} = P^{-1}DP$. In Eq. (2.12), we have made use of a round parenthesis to denote the resulting orthogonal vectors according to the following expressions

$$|1) = \frac{1}{\sqrt{2}}(|1\rangle - |2\rangle), \qquad (1|1) \neq 1, \tag{2.14}$$

$$|2) = \frac{1}{\sqrt{2}}(|1\rangle + |2\rangle), \qquad (2|2) \neq 1. \tag{2.15}$$

Furthermore, the normalized basis will be denoted with round parenthesis and a tilde according to

$$\widetilde{|1)} = \frac{1}{\sqrt{1-\epsilon}}|1) = \frac{1}{\sqrt{2}}\frac{1}{\sqrt{1-\epsilon}}(|1\rangle - |2\rangle), \qquad \widetilde{(1|}\widetilde{|1)} = 1, \tag{2.16}$$

$$\widetilde{|2)} = \frac{1}{\sqrt{1+\epsilon}}|2) = \frac{1}{\sqrt{2}}\frac{1}{\sqrt{1+\epsilon}}(|1\rangle + |2\rangle), \qquad \widetilde{(2|}\widetilde{|2)} = 1. \tag{2.17}$$

In this new basis, $H = E_{\rm A}\widetilde{|1)}\widetilde{(1|} + E_{\rm S}\widetilde{|2)}\widetilde{(2|}$ is already diagonal, with eigenvalues

$$E_{\rm A} \equiv E_1 = \frac{1+2\epsilon}{1+\epsilon}\left(E_0 + \Delta\right), \qquad E_{\rm S} \equiv E_2 = \frac{1-2\epsilon}{1-\epsilon}\left(E_0 - \Delta\right). \tag{2.18}$$

It is important to note the state labeled by 1 corresponds to the antisymmetric state (higher energy) whereas the state 2 is the symmetric one (lower energy). The splitting of these energy levels as a function of couplings and distances is shown in Figs. 2.6 and 2.7. There, one can appreciate that such levels separate asymmetrically from the degenerate bound state energy value as the couplings and overlap parameter increase. It is important to point out that this effect emerges *without having to resort to the introduction of next-nearest-neighbors*, something that cannot be done in this problem.

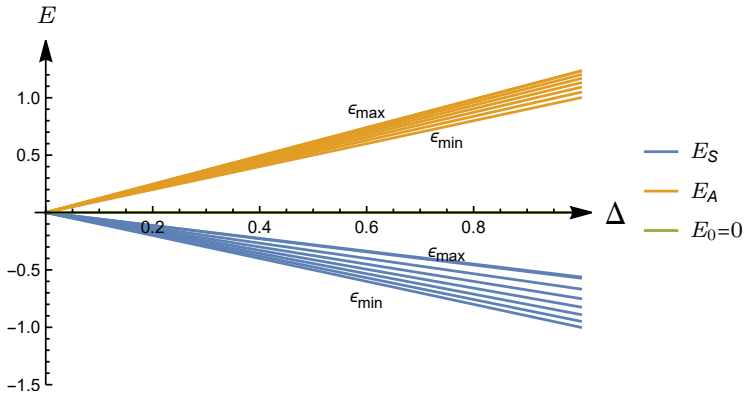

Figure 2.6: Spectral asymmetry as a function of couplings with ϵ as an independent parameter, $\epsilon_{\min} = 0$ and $\epsilon_{\max} = 0.305$.

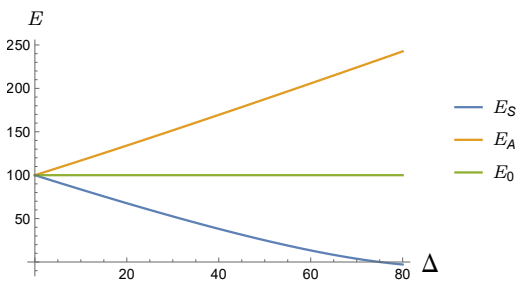

(a) Energy levels as a function of couplings between wells. We took ϵ proportional to Δ and $\epsilon < \Delta/E_0$.

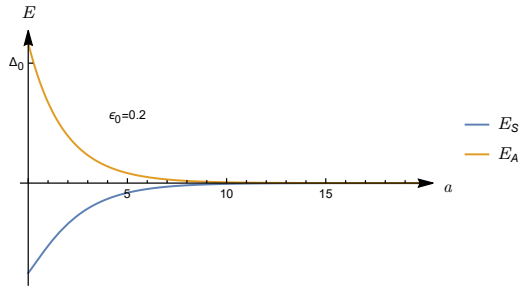

(b) Energy levels as a function of separation between wells, with ϵ proportional to Δ. $\Delta = \Delta(a)$ and $\epsilon = \epsilon(a)$ are given in Eqs. (2.25) and (2.26).

Figure 2.7: Double well energy splitting. In panel (a) we see that the lowest energy levels open in an asymmetrical manner. Panel (b) shows that the spectral asymmetry is enhanced as the distance between wells decreases.

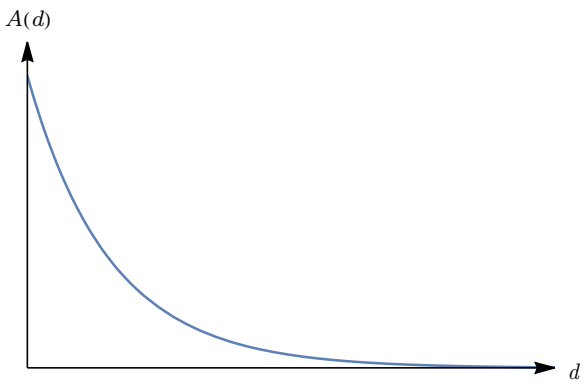

Figure 2.8: Spectral asymmetry as a function of the distance between wells, as measured from the edges.

To quantify how asymmetric or deformed the spectrum is with respect to the isolated resonance, we can make use of the following function

$$A(d) = \frac{||E_1 - E_0| - |E_2 - E_0||}{|E_1 - E_0| + |E_2 - E_0|}, \tag{2.19}$$

a definition that has the attribute of being invariant under the interchange of E_i, $i = 1, 2$. The dependence of A with separation between potential wells is hidden in the expressions for the energy levels, given by Eq. (2.18), for which Δ is given by Eq. (2.25). Figure 2.8 shows the behavior of A for the dimer. As the splitting between energies becomes equal, in the regime of long distances, the asymmetry of the spectrum disappears. On the other hand, when potential wells get close, A grows exponentially.

2.4 Quantum emulation with dielectric media

In the regime where one can approximate the dynamics of electromagnetic fields in cavities by an effective Schrödinger equation, see Ref. [30], section II. A. 3, all of our considerations so far can be tested. This is briefly discussed in the following lines.

2.4.1 Electromagnetic-to-quantum analogy in 1D

In this part we are going to approximate the dielectric cylinders involved in the experiment, described in Fig. 2.1, by a pair of dielectric slabs, see Fig. 2.9. This approximation constitutes a source of inaccuracy, nonetheless this simple treatment has shown good agreement between theoretical predictions and experimental data as can be seen in

Fig. 2.2. The corresponding problem with cylindrical symmetry can be worked out as well, but we proceed with a 1D model for simplicity. We start by considering the Helmholtz wave equation,

$$\nabla^2\mathbf{E} + \frac{\mu\varepsilon\left(\mathbf{r}\right)\omega^2}{c^2}\mathbf{E} + \nabla\left[\frac{1}{\varepsilon(\mathbf{r})}\mathbf{E}\cdot\boldsymbol{\nabla}\varepsilon(\mathbf{r})\right] = 0, \quad \mathbf{E}\perp\boldsymbol{\nabla}\varepsilon(y) \tag{2.20}$$

where ε and μ are the relative permittivity[2] and permeability of the medium, respectively, c is the speed of light and ω is the wave's frequency. Due to the geometry, $\mathbf{E}\cdot\nabla\varepsilon = 0$. Then, assuming a TE mode of the form $\mathbf{E} = \phi\left(y\right)e^{ik_z z}\hat{\mathbf{x}}$ and reading $\varepsilon\left(\mathbf{r}\right)$ from Fig. 2.9, it can be shown that the differential equations describing $\phi\left(y\right)$ can be compactly written as

$$\left[-\frac{\partial^2}{\partial y^2} + U_0\Theta(L/2-|y|)\right]\phi(y) = \mathcal{E}\phi(y), \tag{2.21}$$

where Θ is the Heaviside function, and

$$U_0 \equiv \frac{(\varepsilon_2-\varepsilon_1)\omega^2}{c^2} < 0, \qquad \mathcal{E} \equiv \frac{\varepsilon_2\omega^2}{c^2} - k_z^2 = E_{\text{eff}} - k_z^2 < 0. \tag{2.22}$$

Eq. (2.21) constitutes an effective Schrödinger equation.

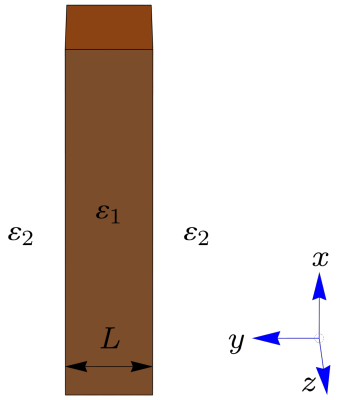

Figure 2.9: Slab with dielectric constant ε_1 inside a medium of permittivity ε_2. A TE mode is assumed for this system. Bound states appear inside the ε_1 region if $\varepsilon_1 > \varepsilon_2$.

In our emulation, the TE mode chosen is the fundamental one, for which $k_x = 0$, as can be obtained from $e^{ik_x x} = 1$ for an infinite slab, or from Neumann conditions, $\cos(k_x x) = 1$, for a finite system bounded by conductive plates in the x direction. In the z direction, a plane wave corresponds to free propagation along optical axis (e.g. optical

[2] ε, the relative permittivity of a medium, must not be confused with ϵ, the overlap parameter.

fibers) for which $k_z > 0$ strictly and $\mathcal{E} < 0$. If, instead, bounding plates are present in $z = 0$ and $z = L_z$, we employ the fundamental mode $\sin(k_z z) = 0$ for which $k_z = \pi/L_z$ guarantees the existence of the trapped wave $\mathcal{E} < 0$. Finally, the expression for the effective energy $E_{\text{eff}} = \dfrac{\varepsilon_2 \omega^2}{c^2}$, is used to change variables from frequency to effective energy so that we could compare the experimental data with the theoretical model.

2.4.2 Effective laws for couplings and overlaps

To complete our analogy, let us consider bound state wavefunctions. We have

$$\phi(y) = \mathcal{N} \cos qy, \quad -L/2 < y < L/2, \tag{2.23}$$

for the inner region of the slab, with $q = \sqrt{|U_0| - |\mathcal{E}|}$, and

$$\phi\,(y) = \tilde{\mathcal{N}} \times \begin{cases} \exp\left(-\frac{|y-\frac{L}{2}|}{\lambda}\right) & \text{if } y > \frac{L}{2}, \\ \exp\left(-\frac{|y+\frac{L}{2}|}{\lambda}\right) & \text{if } y < -\frac{L}{2}, \end{cases} \tag{2.24}$$

for the outer region. $\mathcal{N}$ and $\tilde{\mathcal{N}}$ are normalization constants. The penetration depth is given by $\lambda = 1/\sqrt{|\mathcal{E}|}$.

When considering a pair of parallel slabs, separated by a distance d, the evanescent functions in the region between them give place to couplings

$$\Delta(d) = -\langle n|H|n \pm 1\rangle \approx \int_{\frac{L}{2}}^{\frac{L}{2}+d} dy \phi_n \frac{d^2\phi_{n\pm1}}{dy^2} \approx \Delta_0 e^{-d/\lambda} \tag{2.25}$$

and overlaps

$$\epsilon(d) = \langle n|n \pm 1\rangle \approx \int_{\frac{L}{2}}^{\frac{L}{2}+d} dy \phi_n \phi_{n\pm1} \approx \epsilon_0 e^{-d/\lambda}. \tag{2.26}$$

Thus, by adjusting parameters, such as Δ_0, which is proportional to ϵ_0 ($\Delta_0 = \epsilon_0/\lambda^2$), and λ, we have succeeded in emulating the deformed spectrum of a pair of ceramic disks with relative dielectric constant $\varepsilon_2 \approx 36$ [15], as shown in Fig. 2.2. In such a figure, the agreement between the theoretical model, Eq. (2.18), and the experimental data is observed to be good, even in this crude approximation. It is expected that if we had considered the full geometry, i.e. proper cylindrical functions for bound states of a disk, namely Bessel functions (J_0) inside and modified Bessel functions outside (K_0), then the accuracy would improve but not dramatically, given the exponential tail of K_0. Therefore, we find these

considerations sufficient to illustrate the point that the overlapping nature of localized states induce asymmetries in the frequency spectrum of dielectric arrays. It is important to stress once more that the origin of the spectral deformation is due to ϵ and not by the asymmetry induced by the quadratic (not linear) relation $E_{\text{eff}} \sim \omega^2$, Eq. (2.22), as can be shown by estimating the correction caused by the frequency dependence of energies, which results in a small asymmetry due to the appearance of a $1/(\varepsilon_2 - \varepsilon_1)^{3/2} \sim 4.8 \times 10^{-3}$ factor[3].

Having shown that it is possible to explain the experimentally-found spectral deformation of a dimer, in the next chapter we proceed to extend our treatment by considering a periodic array of potential wells.

[3]This approximation would be valid for many other media of high dielectric constants, but the present value was specified by a manufacturer and supplier of ceramic disks, and reported in [15].

Chapter 3

Band asymmetry in translationally invariant systems

In the present chapter the formalism of tight-binding models with non-orthogonal orbitals is applied to a periodic chain. An asymmetrical energy band emerges from these considerations. The resulting dispersion relation is then compared with a deformed band coming from a Kronig-Penney potential, which has an infinite number of them. The comparison is enriched by the further addition of the spectrum produced by a tight-binding model with orthogonal localized states. The limitation of the latter model is discussed and the advantages of the non-orthogonal orbitals approach are underlined. We find pertinent to start our discussion by explaining the presence of a band index in tight-binding models. This is done through the exposition of the mapping of the spectrum produced by an arbitrary periodic potential to a tight-binding chain of infinite neighbors.

3.1 Periodic potentials and tight-binding models

It is well known that periodic potentials lead to energy bands [35]. See Fig. 3.1. States in each of these bands can be characterized by a wavenumber, i.e. quasimomentum q, and a band index, i, namely $|q, i)$. These vectors are orthogonal to each other, as they diagonalize a hermitian energy operator:

$$(k, j|q, i) = \delta(q - k)\delta_{ij}, \tag{3.1}$$

and constitute the Bloch basis. In this basis, the Hamiltonian, H, of a particle moving in a periodic potential, has matrix elements

$$(k, j|H|q, i) = E^i(q)\delta(q-k)\delta_{ij}, \tag{3.2}$$

with $k, q \in [-\pi, \pi]$.

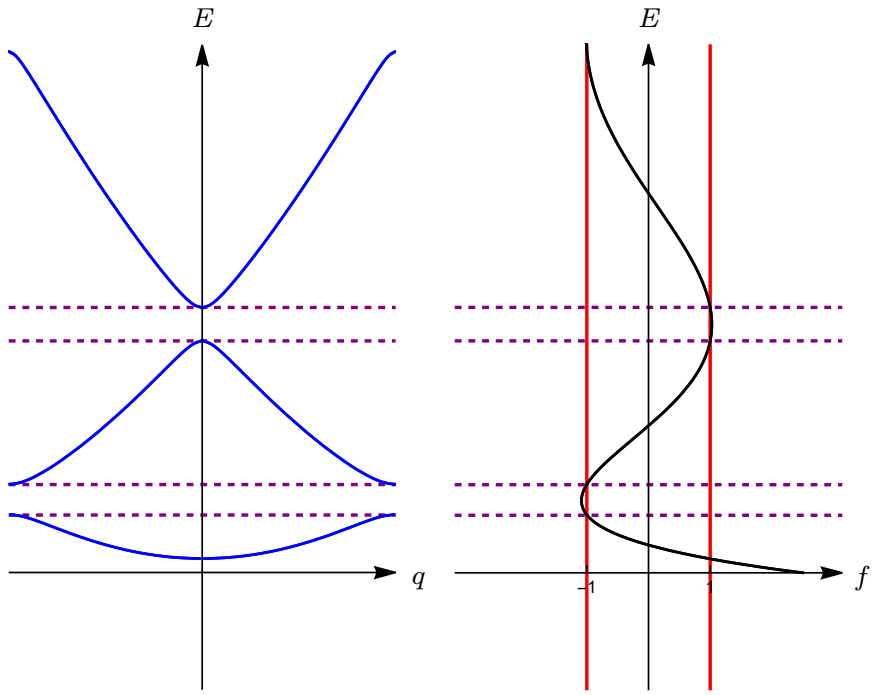

Figure 3.1: Left panel: Energy bands as obtained from Kronig-Penney model. The spectrum corresponds to a potential that consists of a train of delta pulses. Right panel: The black curve represents a simplified version of the right hand side of Eq. (3.24), while the red vertical lines delimit the range of the cosine function, corresponding to the left hand side.

On the other hand, we have bases which are specified by discrete labels, indicating the position in the lattice, $n = 0, \pm1, \pm2, \pm3, \ldots$, and the corresponding band number, $i = 1, 2, 3, \ldots$. The latter is usually omitted when working in a one-band approximation. We identify two sets of states with the same indices in this thesis: the angle-shaped basis, $\{|n, i\rangle\}$, will represent non-orthogonal localized states whereas the round bracket (or parenthesis) basis, $\{|n, i)\}$, will be used throughout this work to denote Wannier states, which are orthogonal to each other; n is given by $n = x/a$, with a being the lattice parameter and

x the continuous position along the chain.

The so-called Wannier states obey

$$(n,i|m,j) = \delta_{nm}\delta_{ij}. \tag{3.3}$$

Introducing T_j, the lattice-translation operator of the j-th band, such that

$$T_j^h|n,j) = |n+h,j), \tag{3.4}$$

with $h \in \mathbb{Z}$, we see that these states are not T_j eigenkets. Neither are energy eigenkets, because H acting on $|m,j)$ has the following effect

$$H|m,j) = \sum_{n=-\infty}^{\infty} \Delta_n^j |m+n,j), \tag{3.5}$$

where Δ_n^j stands for the coupling to the n-th neighbor in the j-th band. Due to translational symmetry, couplings do not depend on the position in the chain. However, couplings connecting neighbors separated by a distinct number of sites, say n and n', are indeed different, hence the subscript n for Δ in the previous expression. We also wish to point out that, in our notation,

$$\Delta_0^j = E_0^j \tag{3.6}$$

is the on-site energy for the j-th band. So, using this set of states, we have

$$(n,i|H|m,j) = \sum_{l=-\infty}^{\infty} \Delta_l^j (n,i|m+l,j) = \sum_{l=-\infty}^{\infty} \Delta_l^j \delta_{n,m+l}\delta_{ij}. \tag{3.7}$$

i.e.

$$(m+l,j|H|m,j) = \Delta_l^j. \tag{3.8}$$

Another way of addressing the previous calculation is by making use of the closure relation of the Bloch basis, namely

$$\begin{aligned}(n,i|H|m,j) &= (n,i|H\sum_{h=1}^{\infty}\int_{-\pi}^{\pi} dq|q,h)(q,h|m,j) \\ &= \sum_h \int dq (n,i|q,h)E^h(q)(q,h|m,j),\end{aligned} \tag{3.9}$$

where the coefficients $(n,i|q,h)$ are Bloch waves[1], which are given explicitly by

$$(n,i|q,h) = \frac{1}{\sqrt{2\pi}} e^{iqn}\delta_{ih}, \tag{3.10}$$

[1]It is easy to see that $(n,i|T|q,h) = e^{-iq}(n,i|q,h) = (n-1,i|q,h)$ has as solution Eq. (3.10).

where the lattice parameter has been set equal to one, i.e. $a = 1$, for simplicity. Thus, upon substitution, we arrive at

$$\begin{aligned}(n,i|H|m,j) &= \sum_h \int dq \frac{1}{\sqrt{2\pi}} e^{iqn}\delta_{ih} E^h(q) \frac{1}{\sqrt{2\pi}} e^{-iqm}\delta_{hj}, \\ &= \delta_{ij}\int dq \frac{1}{\sqrt{2\pi}} e^{iqn} E^j(q) \frac{1}{\sqrt{2\pi}} e^{-iqm}, \\ &= \delta_{ij}\frac{1}{2\pi}\int dq e^{iq(n-m)} E^j(q), \end{aligned} \tag{3.11}$$

and using the fact that only $n = m + l$ and $i = j$ contribute, as found previously, see Eq. (3.7), we finally have

$$(m+l,j|H|m,j) = \frac{1}{2\pi}\int dq e^{iq(m+l-m)}E^j(q) = \frac{1}{2\pi}\int dq e^{iql}E^j(q) = \Delta_l^j, \tag{3.12}$$

where we have recalled Eq. (3.8). This is the expression for the coupling to the l-th neighbor in the j-th band, given as a Fourier transform of the spectrum. So, we can always find Δ's such that a specific E, periodic in q, can be obtained. This important result tells us that we can always map the spectrum of a periodic chain to a tight-binding model with as many neighbors as wished. Of course, in practice we can restrict ourselves to nearest neighbors only, as explained below.

In the light of these results, we write the decomposition of H using a Wannier basis as

$$H = \sum_{l,j} \Delta_l^j |n+l,j)(n,j| =: \sum_{l,j} \Delta_l^j T_j^l \tag{3.13}$$

where we have introduced the definition for lattice-translation operators for arbitrary bands. We see from the previous equations that, if we restrict ourselves to a nearest-neighbor Hamiltonian, then the tight-binding model with dispersion relation

$$E^j_{\mathrm{TB}}(q) = E_0^j + 2\Delta_1^j \cos(q) \tag{3.14}$$

with couplings as in Eq. (3.12), is the best nearest-neighbor tight-binding Hamiltonian that we could possibly come up with to describe the j-th band of the energy spectrum of a periodic system, namely $E^j(q)$. These facts can be employed to compare the energy spectra as predicted by different models such as the non-orthogonal tight-binding model, the orthogonal one, and the Kronig-Penney model. Evidently, the most general result

$$E^j(q) = \sum_{l=-\infty}^{\infty} \Delta_l^j e^{iql}, \quad \Delta^j_{-l} = (\Delta_l^j)^* \tag{3.15}$$

asserts that we can write the dispersion relation $E^j(q)$ as a Fourier series made of the phases e^{iql} and coefficients given by Δ_l^j. There is another subtle observation: Eq. (3.12) allows to see that the contribution to the spectrum from the l-th neighbor in the form of coupling goes as $1/l$ at best. Hence, the usual truncation of the tight-binding energy spectrum to just a few neighbors is justified, in view of the attenuation of further neighbor couplings. The said dependence can be made explicit by a change of variables, just take $u = ql$ in Eq. (3.12), implying $dq = du/l$. Additionally, second neighbors can produce asymmetrical bands.

3.2 Spectral deformation in a periodic system

In the ensuing lines, we are going to solve for the spectrum of a non-orthogonal tight-binding model with the aim of exposing its asymmetric nature and the power of our method. Then, we shall compare our results with the one obtained from a typical matching procedure across boundaries for the Kronig-Penney potential for excited bands, typically non symmetrical with respect to their centers.

Let us consider an infinite system of evenly spaced potential wells. Assuming overlapping localized isolated states, we write the corresponding tight-binding Hamiltonian as

$$H = \Delta \sum_n |n\rangle\langle n+1| + \text{h.c} + E_0 \sum_n |n\rangle\langle n|\,, \tag{3.16}$$

in the one-band approximation, with non-orthogonal kets such that

$$\langle n|n \pm 1\rangle = \epsilon, \quad \langle n|n\rangle = 1. \tag{3.17}$$

A note is in order concerning the presence of ϵ in a dense configuration of potential wells. For certain parameters of the Kronig-Penney model, it is observed that low-lying bands tend to be symmetrical, so Eqs. (3.16) and (3.17) should be intended for the description of higher energy bands. To fix ideas, we may choose $i = 3$, as studied in the next section.

The matrix of inner products turns out to be, by translational symmetry, the following

$$D = \begin{pmatrix} \ddots & \epsilon & 0 & 0 & 0 \\ \epsilon & 1 & \epsilon & 0 & 0 \\ 0 & \epsilon & 1 & \epsilon & 0 \\ 0 & 0 & \epsilon & 1 & \epsilon \\ 0 & 0 & 0 & \epsilon & \ddots \end{pmatrix}. \tag{3.18}$$

The form of Eq. (3.18) suggests that the basis that diagonalizes H and thus D is

$$|\theta) = \sum_n e^{i\theta n} |n\rangle \,. \tag{3.19}$$

These vectors are indeed orthogonal, but not orthonormal:

$$(\theta|\theta') \quad = \quad 2\pi\delta(\theta' - \theta)(1 + 2\epsilon\cos\theta). \tag{3.20}$$

The orthonormal basis in this case will be denoted by a tilde over the state and it is obtained by dividing by the square root of the eigenvalue of D, namely

$$\widetilde{|\theta)} = \frac{1}{\sqrt{2\pi}} \frac{1}{\sqrt{1 + 2\epsilon\cos\theta}} |\theta) = \frac{1}{\sqrt{2\pi}} \frac{1}{\sqrt{1 + 2\epsilon\cos\theta}} \sum_n e^{i\theta n} |n\rangle \,, \qquad \widetilde{(\theta|}\widetilde{|\theta')} = \delta(\theta - \theta'), \tag{3.21}$$

where the band index has been omitted, in such a way that the stationary Schödinger equation $H\widetilde{|\theta)} = E_\theta \widetilde{|\theta)}$ gives the correct energy,

$$E_\theta = E_0(1 + 2\epsilon\cos\theta) + 2\Delta\left[\cos\theta + \epsilon(1 + \cos 2\theta)\right]. \tag{3.22}$$

We thus see that the non-orthogonality, ϵ, and the $\cos 2\theta$ term go hand in hand. In an effective way, the term $\cos 2\theta$ can be regarded as a second-neighbor contribution although all we have done is simply fix the model by an non-negligible overlap. The resulting expression for E_θ is plotted in the next section, and it is compared against bands coming from a tight-binding model with orthogonal states and the exact Kronig-Penney model.

3.3 Asymmetric spectrum in the Kronig-Penney model vs deformed tight-binding bands

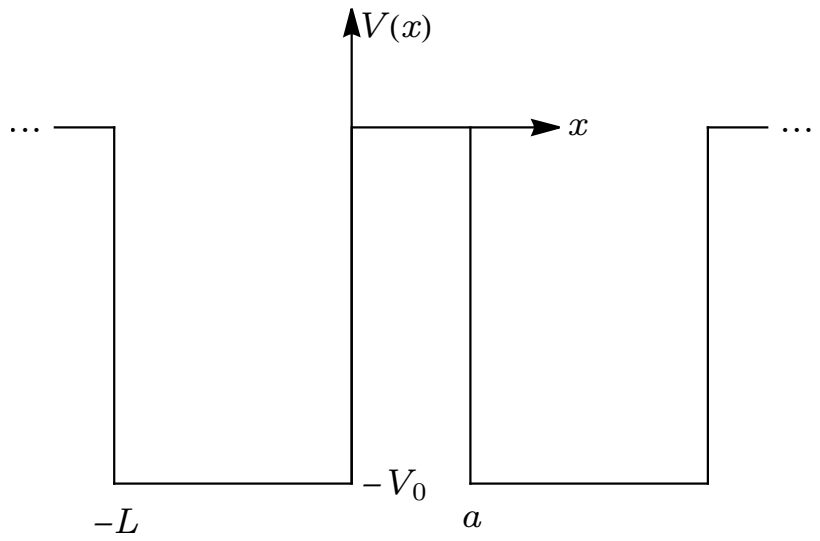

Figure 3.2: Kronig-Penney potential. Infinite chain of potential wells of depth $-V_0$ and width L separated a distance a.

Let us start by defining the Kronig-Penney potential [28], which is illustrated in Fig. 3.2. The function that characterizes the system is periodic, with period equal to $L+a$, where L is the width of the potential wells and a is the distance between consecutive potential wells measured from the edges. We have

$$V(x) = \begin{cases} -V_0, & \text{if } x \in \Omega_1 := (-L, 0), \\ 0, & \text{if } x \in \Omega_2 := (0, a). \end{cases} \tag{3.23}$$

The method of smooth matching of the wavefunction and its derivative at the discontinuities of the potential, as well as the use of Bloch's theorem with quasimomentum q, gives the condition

$$\cos q(a+L) = \cos \alpha L \cos ka - \frac{k^2+\alpha^2}{2k\alpha} \sin \alpha L \sin ka, \tag{3.24}$$

where $\alpha = \sqrt{V_0 + k^2}$ and $k^2 = E > 0$. The case $E < 0$ can be studied by changing $k \to ik$.

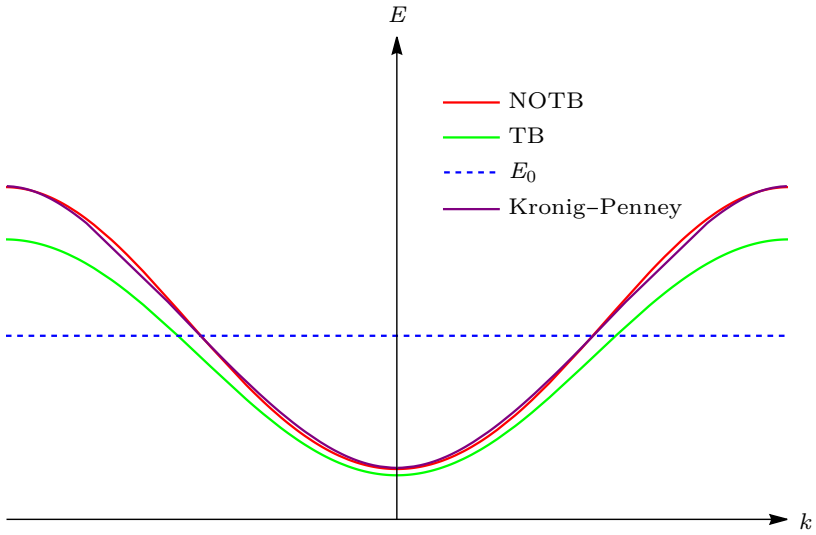

Figure 3.3: Comparison between the exact spectrum of the Kronig-Penney model versus those obtained from tight-binding models with both orthogonal and non-orthogonal localized states. The third band of the energy spectrum has been chosen for the comparison.

As it is shown in Fig. 3.3, it is possible to find values for the a, L and V_0 parameters such that the energy bands show an asymmetry between its lower and upper part, which can only be described with corrected tight-binding models. These corrections could come from overlapping orbitals or from multiple neighbors. As we have shown in the previous section, the treatment with non-orthogonal orbitals for dense arrays gave rise to correcting factors in the spectrum that depend on ϵ. The agreement in Fig. 3.3 is excellent. It will be our job to extend these treatments to non-periodic potential well configurations in the development of this thesis.

Chapter 4

Wannier functions for chains with overlapping orbitals

The present chapter deals with Wannier functions (WFs), which are explicitly obtained for a pair of systems: the dimeric array of potential wells and a translationally invariant structure. We start with the simplest of these cases, i.e., the WFs for the double square well. Then, we review the Wannier transform in order to estimate WFs for a periodic configuration of potential wells. The kernel of the Wannier transform is further studied by choosing two types of modulating functions which gives rise to WFs of different shapes.

4.1 Wannier functions for a dimer

As anticipated in the preamble, we begin by defining the WFs for a system consisting of only two potential wells; this result, although simple, aids to gain physical intuition about the shape of WFs. By discrete-Fourier-transforming the orthonormal basis, Eq. (2.16), we arrive at the Wannier states corrected by the non-orthogonality of atomic orbitals, namely

$$|w_L) = \frac{1}{2}\left(\frac{1}{\sqrt{1-\epsilon}} + \frac{1}{\sqrt{1+\epsilon}}\right)|1\rangle + \frac{1}{2}\left(\frac{1}{\sqrt{1+\epsilon}} - \frac{1}{\sqrt{1-\epsilon}}\right)|2\rangle\,, \tag{4.1}$$

$$|w_R) = \frac{1}{2}\left(\frac{1}{\sqrt{1+\epsilon}} - \frac{1}{\sqrt{1-\epsilon}}\right)|1\rangle + \frac{1}{2}\left(\frac{1}{\sqrt{1-\epsilon}} + \frac{1}{\sqrt{1+\epsilon}}\right)|2\rangle\,, \tag{4.2}$$

which for small ϵ reduce to

$$|w_L) = |1\rangle - \frac{\epsilon}{2}|2\rangle \qquad |w_R) = |2\rangle - \frac{\epsilon}{2}|1\rangle\,, \tag{4.3}$$

making evident the small correction introduced by the non-orthogonal nature of the localized basis (see Fig. 4.1). The orthogonality property can be easily checked by projecting kets between each other. We learn from this simple example that WFs do not differ a lot from isolated states in a dilute regime of potential wells. When this is not the case, WFs acquire an oscillating exponential tail in order to ensure orthogonality with its neighboring function.

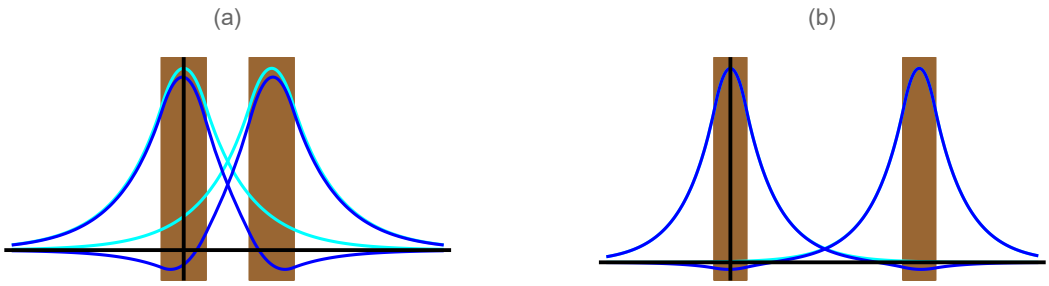

Figure 4.1: WFs (dark blue) for a dimer to first order in ϵ. (a) WFs for small potential well interdistance. In this regime, WFs differ notoriously from ground state wavefunctions (cyan) of isolated potential wells. The latter are represented by brown regions. (b) WFs for wells far apart. The more separated the wells are, the more WFs resemble isolated bound states. This color code will be used throughout this chapter.

4.2 The case of periodic arrays

Here, after the introductory yet important example of the calculation of WFs for a pair of disks modeled by two potential wells, we proceed to explain the procedure for obtaining WFs for a periodic system. Given a localized non-orthogonal basis $\{|n\rangle\}$ and a discrete translation operator, T, with eigenstates $|\theta)$, we can write

$$|\theta) = \sum_n c_n \, |n\rangle \, . \tag{4.4}$$

Using the translational symmetry, $[H, T] = 0$, it can be shown that $c_n = e^{in\theta}$, just as we did in the previous chapter. There, it was shown how to normalize such basis, see section 3.2. By recalling Eq. (3.21), written as

$$\widetilde{(\theta|}\widetilde{|\theta')} \;\; = \;\; |\mathcal{N}|^2 2\pi\delta(\theta' - \theta)(1 + 2\epsilon\cos\theta) = \delta(\theta - \theta'), \tag{4.5}$$

we note that we can introduce any complex number of unit modulus in the normalization constant, $\mathcal{N}$. This may include functions of θ, in general, $e^{if(\theta)}$, which gives

$$\mathcal{N} = \frac{1}{\sqrt{2\pi}} \frac{e^{if(\theta)}}{\sqrt{1+2\epsilon\cos\theta}}. \tag{4.6}$$

The phase $e^{if(\theta)}$ embodies a degree of freedom in the definition of WFs for the system under study, a point that shall be revisited in further sections. Thus, we can rewrite Eq. (4.4) normalized as

$$\widetilde{|\theta)} = \frac{1}{\sqrt{2\pi}} \sum_m \frac{e^{i(m\theta+f(\theta))}}{\sqrt{1+2\epsilon\cos\theta}} |m\rangle \,. \tag{4.7}$$

The Fourier transform, $\mathcal{F}$, is a unitary operation and it preserves orthogonality. Hence, the application of $\mathcal{F}$ on $\widetilde{|\theta)}$ does not land on the non-orthogonal basis $\{|n\rangle\}$. We rather introduce the round bracket notation for orthogonal states

$$\begin{aligned} |n) &= \frac{1}{\sqrt{2\pi}} \int_{-\pi}^{\pi} d\theta e^{-in\theta} \widetilde{|\theta)} = \frac{1}{2\pi} \int_{-\pi}^{\pi} d\theta e^{-in\theta} \sum_m \frac{e^{i(m\theta+f(\theta))}}{\sqrt{1+2\epsilon\cos\theta}} |m\rangle \\ &= \frac{1}{2\pi} \sum_m |m\rangle \int_{-\pi}^{\pi} d\theta \frac{e^{i[(m-n)\theta+f(\theta)]}}{\sqrt{1+2\epsilon\cos\theta}}, \end{aligned} \tag{4.8}$$

obtained from Fourier transforming the orthogonal Bloch states. The band index has been omitted for simplicity, but can be restored in the kets, e.g. $|m\rangle \to |m,i\rangle$. In a compact way, by defining the kernel of the transform as

$$K_{m-n} = \frac{1}{2\pi} \int_{-\pi}^{\pi} d\theta \frac{e^{i(m-n)\theta+if(\theta)}}{\sqrt{1+2\epsilon\cos\theta}} \tag{4.9}$$

we can restate the previous result as

$$|n) = \sum_{m=-\infty}^{\infty} K_{m-n} |m\rangle \,. \tag{4.10}$$

This operation, which takes as input non-orthogonal localized isolated states and gives back a set of vectors orthogonal to each other, is known as the Wannier transform of $|m\rangle$. In the following pages, the kernel will be evaluated for some phases, but before doing this, we review an important property of WFs.

4.2.1 Wannier functions: translation invariance property

When projecting a Wannier state, Eq. (4.10), to position space, one obtains a WF, namely

$$W_n(x) := \langle x|\, n) = \sum_{m=-\infty}^{\infty} K_{m-n} \langle x|m\rangle \,, \tag{4.11}$$

where $\phi_m(x) := \langle x|m\rangle$ is the wavefunction for the non-orthogonal orbital. In a 1D periodic lattice, isolated atomic orbitals are translationally invariant, namely

$$\phi_m(x) = \phi_0(x - am), \quad \phi_0(x) = \phi(x), \tag{4.12}$$

where a is the lattice parameter and the ground state wavefunction centered at the origin, $\phi(x)$, can be seen in Fig. 4.1 (cyan colored). The aforementioned property is inherited by WFs. To show that this is indeed the case, define $q = m - n$, and rewrite Eq. (4.11) as

$$W_n(x) = \sum_{q=-\infty}^{\infty} K_q \phi(x - aq - an). \tag{4.13}$$

Finally, we define $W_0(x) := \sum_q K_q \phi_0(x - aq)$ as the WF centered at the origin, such that $W_n(x)$, given by Eq. (4.13), is obtained by translating the function just defined. WFs are orthogonal by construction, $(m|n) = \delta_{mn}$, and this statement is equivalent to

$$\int_{-\infty}^{\infty} W_0^*(x - am) W_0(x - an) dx = \delta_{mn}, \tag{4.14}$$

where we have used Eq. (4.13).

4.3 Estimating Wannier functions

We now want to evaluate the kernel K_{m-n} for a couple of phases, which have the effect of making the WFs broader or narrower as well as changing its shape, thus producing different types of localization. Recalling

$$K_{m-n} = \frac{1}{2\pi} \int_{-\pi}^{\pi} d\theta \frac{e^{i(m-n)\theta + if(\theta)}}{\sqrt{1 + 2\epsilon \cos\theta}}, \tag{4.15}$$

where $m - n$ is the discrete position difference, $f(\theta)$ embodies the freedom of phase in the definition of the transform, the denominator represents the normalization adjustment due to lack of orthogonality, and $1 \gg \epsilon > 0$. Note that if $f \to 0$ and $\epsilon \to 0$, then $K_{m-n} \to \delta_{nm}$, as expected. So, in the following, by picking out some functions with critical points for f, it is shown that one can obtain WFs of different shapes all obeying the orthogonality condition. It is important to note that the problem of maximally localized WFs has been solved in 1D [36], although the question is still open in higher dimensions. WFs are relevant for understanding electronic distributions in atoms or electromagnetic radiation around obstacles. This important basis has become relevant in the field of computational condensed matter physics, specifically in the study of electronic properties of materials.

4.3.1 Wannier functions without modulation: the case $f(\theta) = 0$

In this section we are going to exploit the fact that the correcting factor due to non-orthogonality, given by

$$\frac{1}{\sqrt{1+2\epsilon\cos\theta}}, \tag{4.16}$$

can be expanded in a Taylor series in order to evaluate the Wannier transform for the case $f(\theta) = 0$. Here, it will result useful the fact that $\cos^2\theta$ can be written in terms of $\cos 2\theta$ and $\cos\theta$ and similarly for higher powers of $\cos\theta$. By taking advantage of the previous observation, we are led to the Fourier transform of $\cos^k\theta$ as being equal to

$$\int_{-\pi}^{\pi} d\theta e^{iq\theta}\cos^k\theta = 2\pi\begin{cases} 0, & \text{if } k-q \text{ is odd} \\ \binom{k}{\frac{k-q}{2}}\frac{1}{2^k} = \frac{2^{-k}k!}{(\frac{k-q}{2})!(\frac{k+q}{2})!}, & \text{if } k-q \text{ is even,} \end{cases} \tag{4.17}$$

where q should be understood as $m-n$; this identity can be found in Appendix B. Then, we expand the correcting factor as a Taylor series around $\epsilon = 0$,

$$\begin{aligned} \frac{1}{\sqrt{1+2\epsilon\cos\theta}} &= 1 - \frac{1}{2}2\epsilon\cos\theta + \frac{3!!}{2!2^2}4\epsilon^2\cos^2\theta + \dots \\ &= \sum_{n=0}^{\infty}\frac{(-)^n(2n-1)!!}{n!2^n}(2\epsilon)^n\cos^n\theta, \end{aligned} \tag{4.18}$$

where the double factorial notation has been employed. Now, the kernel can be evaluated by substituting the previous identities in Eq. (4.15), the result being

$$\begin{aligned} 2\pi K_q &= \int_{-\pi}^{\pi} d\theta e^{iq\theta}\sum_{k=0}^{\infty}\frac{(-)^k(2k-1)!!}{k!2^k}(2\epsilon)^k\cos^k\theta \\ &= \sum_{k=0}^{\infty}\frac{(-)^k(2k-1)!!}{k!2^k}(2\epsilon)^k\begin{cases}\frac{2\pi}{2^k}\frac{k!}{\left(\frac{k-q}{2}\right)!\left(\frac{k+q}{2}\right)!} & \text{if } k-q \text{ is even,} \\ 0, \quad \text{otherwise.}\end{cases} \end{aligned}$$

The result just obtained is useful for evaluating Eq. (4.11), or (4.13). For example, we have

$$K_0 = 1, \qquad K_{\pm 1} = -\frac{\epsilon}{2}, \tag{4.19}$$

as nearest-neighbors contributions. This leads to

$$W_n(x) \approx \phi_n(x) - \frac{\epsilon}{2}\left[\phi_{n-1}(x) + \phi_{n+1}(x)\right]. \tag{4.20}$$

We see that the kernel, K, takes a few of the neighboring wavefunctions and subtracts them from the localized on-site orbital. Figure 4.2 shows the resulting WF according to Eq. (4.20). In such figure, contributions to the shape of the WF arise only from nearest-neighbor isolated states. In fact, WFs can be estimated to higher orders of ϵ, for example, Fig. 4.3 depicts WFs up to 2nd order in ϵ. Of course, higher powers of ϵ become each time smaller, thus we can drop further terms from our considerations.

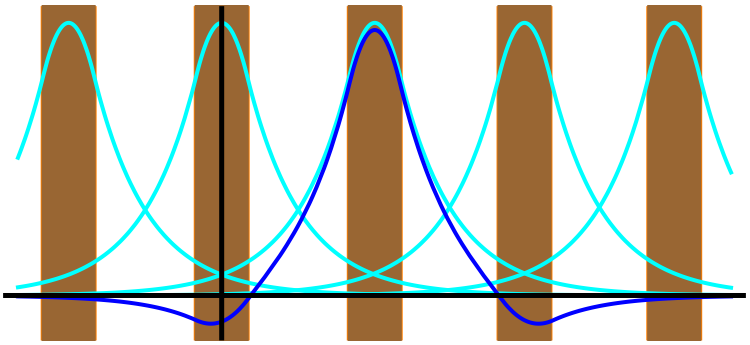

Figure 4.2: WF (dark blue) to first order in ϵ for a periodic system, without modulation. The transform responsible for producing such function modifies the on-site non-orthogonal ket by adding to it neighboring states weighed by the small overlap, ϵ.

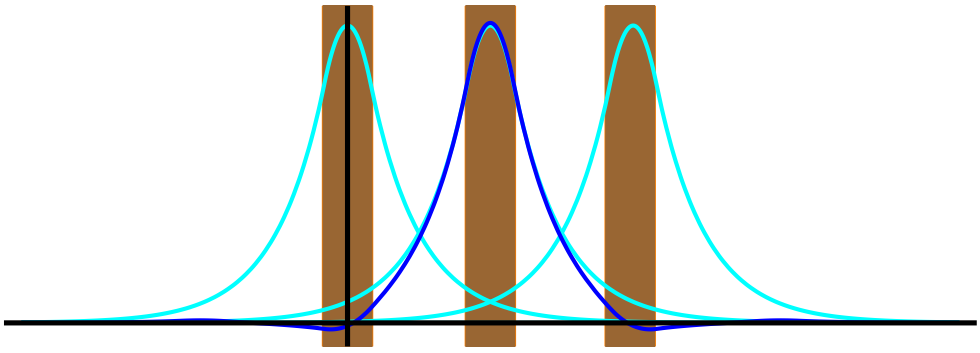

Figure 4.3: WF to second order in ϵ, i.e. with next-to-nearest neighbors contributions. It can be seen that this WF oscillates twice.

4.3.2 Stationary phase approximation for $f(\theta) \neq 0$

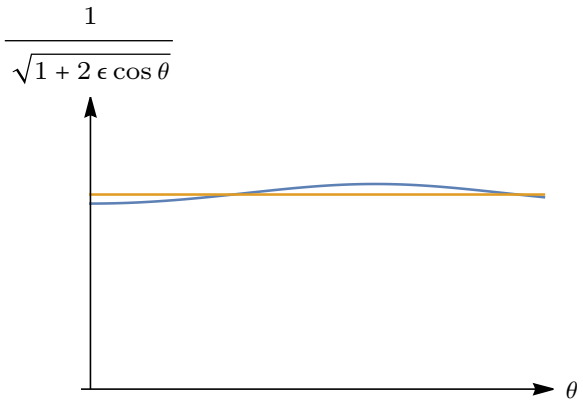

Figure 4.4: The correcting factor, $1/\sqrt{1+2\epsilon\cos\theta}$, is drawn in blue. This term, originated from normalizing a non-orthogonal basis, does not oscillates significantly. In orange, the constant function equal to 1 is shown. Thus, the term $e^{i(q\theta+f(\theta))}$, appearing in the kernel of the Wannier transform, dominates the oscillations of the integrand. The value of ϵ is 0.05.

The previous calculation was carried out while ignoring the modulation $f(\theta)$. This time, let us consider a non-zero function for the computation of WFs. To preserve the limit $\delta_{m,n}$ when $\epsilon \to 0$ (bona fide) we take $f(\theta) = \epsilon g(\theta)$ so that $f \to 0$ for a vanishing overlap and introduce $g(\theta)$ such that it has a minimum at $\theta = 0$, inside the interval $[-\pi, \pi]$ (first Brillouin zone). As an example, we choose $f(\theta) = \epsilon\alpha\theta^2$, where α is an adjustable parameter. The quadratic form of f guarantees the existence of a stationary point for the phase. Figure 4.4 illustrates the fact that the correcting factor due to non-orthogonality does not oscillate significantly, which means that the term $e^{i(q\theta+f(\theta))}$ dominates the oscillations of the integrand in the kernel of the Wannier transform, Eq. (4.15). So, we can use the stationary phase approximation in order to evaluate the following integral

$$K_q = \frac{1}{2\pi}\int_{-\pi}^{\pi} d\theta \frac{e^{i(q\theta+\epsilon\alpha\theta^2)}}{\sqrt{1+2\epsilon\cos\theta}}. \tag{4.21}$$

The phase in Eq. (4.21), defined as $\Phi := q\theta + \epsilon\alpha\theta^2$, has a stationary point at $\theta^* = -\frac{q}{2\epsilon\alpha}$, which can be easily shown by solving $\Phi'(\theta) = 0$. This last observation, enables us to approximate the integral to

$$K_q \approx \frac{1}{2\pi}\frac{e^{-i\frac{q^2}{4\epsilon\alpha}}}{\sqrt{1+2\epsilon\cos\left(\frac{q}{2\epsilon\alpha}\right)}}\int_{-\pi}^{\pi} d\theta e^{i\epsilon\alpha(\theta+\frac{q}{2\epsilon\alpha})^2}, \tag{4.22}$$

where we have Taylor expanded the phase up to second order in θ, around the stationary point, and have dropped higher order terms; we also have approximated the correcting factor by its value at θ^*. There are two cases

$$-\pi < \theta + \frac{q}{2\epsilon\alpha} < \pi \quad \text{or} \quad \left|\theta + \frac{q}{2\epsilon\alpha}\right| > \pi. \tag{4.23}$$

In the first case, we can approximate the integral in Eq. (4.22), by

$$\int_{-\infty}^{\infty} d\theta e^{i\epsilon\alpha\theta^2} = \sqrt{\frac{\pi}{i\epsilon\alpha}}, \tag{4.24}$$

and in the second case we take the integral previously referred as equal to zero since the stationary point falls outside the integration region. This leads to the following estimation for the kernel,

$$K_{m-n} \approx \frac{1}{2\pi} \frac{e^{-i\frac{(m-n)^2}{4\epsilon\alpha}}}{\sqrt{1+2\epsilon\cos\left(\frac{m-n}{2\epsilon\alpha}\right)}} \begin{cases} \sqrt{\frac{\pi}{i\epsilon\alpha}}, & \text{if} \quad -\pi < \dfrac{m-n}{2\epsilon\alpha} < \pi \\ 0 \quad \text{otherwise,} \end{cases} \tag{4.25}$$

when $f(\theta) = \epsilon\alpha\theta^2$. This produces a highly oscillatory WF, which is approximately given by

$$\begin{aligned} W_n(x) &\approx \sum_{m=n-[2\pi\epsilon\alpha]}^{n+[2\pi\epsilon\alpha]} \frac{e^{-\frac{i(m-n)^2}{4\epsilon\alpha}}}{2\sqrt{i\pi}} \sqrt{\frac{1}{\epsilon\alpha + 2\epsilon^2\alpha\cos\left(\frac{m-n}{2\epsilon\alpha}\right)}} \phi_m(x) \\ &\approx \frac{1}{2\sqrt{\pi i\epsilon\alpha}} \sum_{m=n-[2\pi\epsilon\alpha]}^{n+[2\pi\epsilon\alpha]} e^{-\frac{i(m-n)^2}{4\epsilon\alpha}} \phi_m(x), \end{aligned} \tag{4.26}$$

where we have dropped terms of second order in epsilon in the last expression. We note from Eq. (4.26) that the phases, responsible for weighing the contributions to the resulting WF from non-orthogonal orbitals, oscillate considerably because ϵ is a small parameter. A collection of WFs for this case is presented in Fig. 4.5.

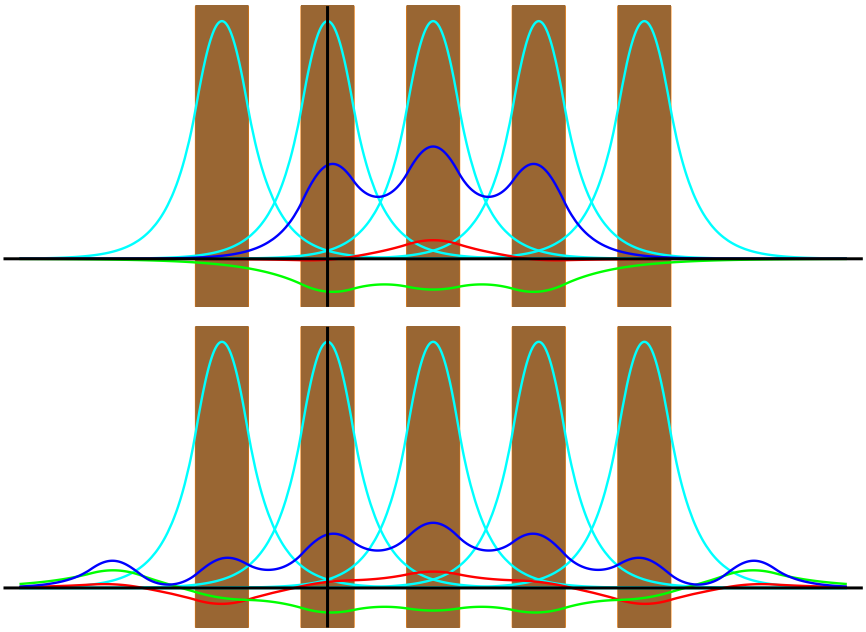

Figure 4.5: Resulting WFs from a stationary phase approximation. A quadratic phase in θ was used to ensure the existence of a non-trivial critical point for the phase Φ. Color code: Dark blue - squared modulus of WF, red/green - real/imaginary part of $W_n(x)$. Probability distributions from non-orthogonal localized states are shown in cyan. The top panel has a lower value for α making the WF narrower than the bottom panel.

4.3.3 Wannier function from a trigonometric phase

So far, we have calculated WFs for an infinite chain of evenly spaced potential wells both with and without a modulating phase. As another example of the latter case, let us explore a trigonometric phase instead of the polynomial one employed in the previous section. We start with

$$K_q = \frac{1}{2\pi}\int_{-\pi}^{\pi} d\theta \frac{e^{i(q\theta+\alpha\epsilon\cos\theta)}}{\sqrt{1+2\epsilon\cos\theta}}, \tag{4.27}$$

where we have introduced $f(\theta) = \alpha\epsilon\cos\theta$. The evaluation of this integral is actually straightforward. We start by Taylor-expanding the correcting factor, which is something we have previously done, see Eq. (4.18). Thus, we write

$$K_q = \frac{1}{2\pi}\int_{-\pi}^{\pi} d\theta e^{i(q\theta+\alpha\epsilon\cos\theta)} \sum_{k=0}^{\infty} (-)^k \frac{C_k^{2k-1}}{2^{2k-1}} 2^k \epsilon^k \cos^k\theta, \tag{4.28}$$

where C_k^{2k-1} stands for the binomial coefficient which appears due to its relation to the double factorial, namely $C_k^{2k-1} = (2k-1)!!2^{k-1}/k!$. Recalling Jacobi-Anger's identity [38], and the cosine series expansion

$$e^{i\eta\cos\theta} = \sum_{l=-\infty}^{\infty} i^l J_l(\eta) e^{il\theta}, \qquad \cos^k\theta = \frac{e^{-ik\theta}}{2^k}\sum_{r=0}^{k} C_r^k e^{2ir\theta} \tag{4.29}$$

and substituting both results in Eq. (4.28), we are led to

$$K_q = \frac{1}{2\pi}\sum_{k=0}^{\infty}\sum_{r=0}^{k}(-)^k \frac{C_k^{2k-1}}{2^{2k-1}} 2^k \epsilon^k \frac{1}{2^k} C_r^k \int_{-\pi}^{\pi} e^{i\{(q+2r-k)\theta+\alpha\epsilon\cos\theta\}} d\theta \tag{4.30}$$

and by making use of Eq. (4.29), the integral evaluates to

$$\int_{-\pi}^{\pi} e^{i\{(q+2r-k)\theta+\alpha\epsilon\cos\theta\}} d\theta = 2\pi i^{k-q-2r} J_{k-q-2r}(\alpha\epsilon) \tag{4.31}$$

thus, the sum turns out to be

$$K_q(\alpha,\epsilon) = \sum_{k=0}^{\infty}\sum_{r=0}^{k}(-)^k \frac{C_k^{2k-1}}{2^{2k-1}} \epsilon^k C_r^k i^{k-q-2r} J_{k-q-2r}(\alpha\epsilon). \tag{4.32}$$

This is our most general answer for the kernel of the Wannier transform when considering a trigonometric phase.

Let us study the case when $\alpha \to 0$, which makes use of the property $J_l(0) = \delta_{l,0}$, translating into

$$K_q(0,\epsilon) = \sum_{k=0}^{\infty} \frac{(-)^k}{2^{2k-1}} \epsilon^k C_k^{2k-1} C_{(k-q)/2}^k, \tag{4.33}$$

if $k-q$ is even, and the summand is zero otherwise. One of the binomial coefficients, $C_{(k-q)/2}^k$, shows that the most significant contribution is for $q = 0$. An additional point to have in mind is the power of ϵ, since it also limits contributions to the kernel. Because ϵ is small, few values of k are enough to get a good approximation. The resulting kernel, Eq. (4.33), in the limit just discussed is in full agreement with the result without modulation, Eq. (4.19), as expected.

Now, consider the limit $\alpha\epsilon \gg 1$, with $\epsilon \ll 1$ in Eq. (4.32). The caustics of the Bessel function, $J_{k-q-2r}(\alpha\epsilon)$, are approximately delimited by the interval $-\alpha\epsilon \lesssim k-q-2r \lesssim \alpha\epsilon$ [31]. We can restrict ourselves to positive-indexed Bessel functions because $J_{-l} = (-)^l J_l$. Moreover, we cut the infinite sum in Eq. (4.32) to the N-th order in ϵ, i.e.

we restrict $k \leq N$, then, we find the following inequalities satisfied by all the variables that come into play

$$N - q - 2r \lesssim \alpha\epsilon, \qquad N - m + n - 2r \lesssim \alpha\epsilon \tag{4.34}$$

and solving for the neighbor index, we find that it satisfies

$$m \gtrsim n - 2r + N - \alpha\epsilon. \tag{4.35}$$

From the last equation, it is seen that m is bounded in this approximation, thus estimating the number of neighbors that contribute to creating the resulting WF. To lowest order in ϵ for the correcting factor, i.e. $k = 0$, we can use the asymptotic form of J_l for large argument, since $\alpha\epsilon \gg 1$, $\epsilon \ll 1$, obtaining

$$K_q(\alpha\epsilon) = 2i^q J_q(\alpha\epsilon) \sim 2i^q \sqrt{\frac{2}{\pi\alpha\epsilon}} \cos\left(\alpha\epsilon - \frac{q\pi}{2} - \frac{\pi}{4}\right), \tag{4.36}$$

where $|q| \lesssim \alpha\epsilon$, in this case. In particular,

$$n = 0, \implies |m| \lesssim \alpha\epsilon \tag{4.37}$$

obtaining an oscillatory sum

$$W_0(x) = 2 \sum_{m=-[\alpha\epsilon]}^{[\alpha\epsilon]} i^m \sqrt{\frac{2}{\pi\alpha\epsilon}} \cos\left(\alpha\epsilon - \frac{m\pi}{2} - \frac{\pi}{4}\right) \phi(x - ma). \tag{4.38}$$

Such oscillatory solution behaves as depicted in Fig. 4.6. In this case, the width of the WF is controlled by the α parameter.

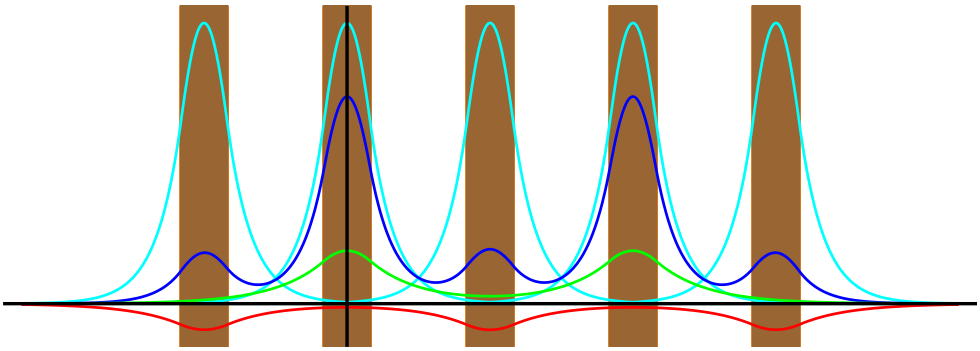

Figure 4.6: $|W_n(x)|^2$ (dark blue) obtained from a kernel with cosinusoidal phase with its real (imaginary) part shown in red (green). The number of non-orthogonal states that make up a WF is controlled by the α parameter.

We have shown that it is possible to compute WFs for dense arrays of potential wells for which overlapping of atomic orbitals cannot be ignored. In the dimeric case, WFs consists of modified localized non-orthogonal isolated states in such a way that they acquire oscillating exponential tails to ensure orthogonality between each other. On the other hand, in a dilute regime, we saw that WFs resemble isolated states, thus justifying the usual tight-binding approach with orthogonal orbitals.

Regarding compact periodic potential well structures, it is possible to calculate WFs from the Wannier transform. This operation requires of the evaluation of a Kernel which in turn has an ambiguity in his definition, we refer to the freedom of phase that was explored throughout this chapter. Starting from an unmodulated WF, to first and second order in ϵ_0, we then considered two different phases for the transform. The first one, a quadratic function, gave rise to a stationary point in the phase from which a highly oscillatory WF emerged. The second modulating function was trigonometric and it led to a WF whose width was controlled by the parameter α there introduced. All of these resulting bases both in the dimeric and periodic cases were obtained by taking into account the non-orthogonal nature of atomic states.

Chapter 5

Equispaced spectra from non-orthogonal orbitals: towards an electronic clock

In the present chapter, it is explained how to obtain a desired energy spectrum for 1D lattices for which the overlap between nearest-neighbor atomic states cannot be ignored. We start from a generalized eigenvalue equation for non-orthogonal localized states, which enables the design of compact arrays with equispaced energy levels. After implementing both the required coupling law and on-site potential, and evaluating the spectrum, we introduce the spectral rigidity as a measure of *equispacedness*. We then present an example of an aperiodic chain with approximately evenly spaced energy levels. The evolution is evaluated for a wavepacket, finding a periodic dynamics. Lastly, we discuss the possibility of employing a structure of this type to construct an isochronous electronic device. The working frequency for such a clock is estimated and a comparison is made against other oscillators.

5.1 Secular equation for a deformed spectrum

In this section we are going to introduce an eigenvalue equation written in a basis of non-orthogonal localized states. The energy equation

$$H\left|E\right\rangle = E\left|E\right\rangle, \tag{5.1}$$

which is written in spectral decomposition as

$$H = \sum_E E\,|E\rangle\langle E|\,, \tag{5.2}$$

in the absence of degeneracy, will be our starting point in this discussion. We are going to assume that $H_{mn} = \langle m|H|n\rangle$ is given. However, H_{mn} is not a matrix element in an orthonormal basis. To illustrate the meaning of the previous sentence, take, as an example, the Hamiltonian introduced in Eq. (2.10), namely $H = E_0(|1\rangle\langle 1| + |2\rangle\langle 2|) - \Delta(|1\rangle\langle 2| + |2\rangle\langle 1|)$, where the kets are non-orthogonal. Then, H_{mn} can be computed by using the fact that $\langle m|n\rangle = \delta_{mn} + \epsilon\delta_{m,n+1} + \epsilon\delta_{m,n-1}$. Furthermore, we know that there exists a non-unitary transformation, A, that makes the inner product, encoded in D, orthonormal, i.e. $A^\dagger DA = 1$. In fact, A is such that $|n) = A\,|n\rangle$, where the round (angular) kets stand for orthogonal (non-orthogonal) states, as previously pointed out. This means that $D_{nm} = \langle n|m\rangle = (n|(A^\dagger)^{-1}A^{-1}|m) = (n|(AA^\dagger)^{-1}|m)$ is the hermitian matrix of inner products, thus defining D in terms of A. The spectral decomposition of H, Eq. (5.2), can be multiplied by localized vectors $\langle n|\,,\ |m\rangle\,$, to get

$$\langle n|H|m\rangle \;\;=\;\; \sum_E E\,\langle n|E\rangle\,\langle E|m\rangle\,, \tag{5.3}$$

where, in the right-hand side, we can insert a complete set of orthogonal states and write the non-orthogonal basis in terms of the orthogonal one, through the action of A, such that we end up with

$$\langle n|H|m\rangle \;\;=\;\; \sum_{r,s}(n|A^{\dagger\,-1}|r)\sum_E E(r|E\rangle\langle E|s)(s|A^{-1}|m), \tag{5.4}$$

which has the general form,

$$\langle n|H|m\rangle = \sum_{r,s}(A^{\dagger\,-1})_{nr}(\mathrm{diag}\,\{E\})_{rs}(A^{-1})_{sm}. \tag{5.5}$$

With this, it is straightforward to see that since $D = (AA^\dagger)^{-1}$, as it was shown above, then the secular equation is written as

$$|H - ED| = 0, \tag{5.6}$$

where the matrices H and D are written in the non-orthonormal localized basis.

As an important application of the newly obtained secular equation, we can infer the shape of operators when wavefunctions are of exponential type in interstitial regions,

e.g. square wells. It is recognized that both D and H depend on the geometric array of sites (atoms, potential wells, resonators, etc.) and that the overlap integrals,

$$H_{nm} = \int \phi_n^* H \phi_m dx \simeq \Delta_0 e^{-d_{nm}/\lambda}, \quad n \neq m, \tag{5.7}$$

$$D_{nm} = \int \phi_n^* \phi_m dx \simeq \epsilon_0 e^{-d_{nm}/\lambda}, \quad n \neq m, \tag{5.8}$$

scale in the same way as a function of the distance d_{nm} between sites n, m.

Since $D_{nn} = 1$ and $H_{nn} = E_0$, to zero-th order in the deformation (the original model, a finite oscillator in a dilute regime [17], did not have on-site potential), we propose a tridiagonal matrix, Ω, such that

$$H = \Delta_0 \Omega + E_0 \mathbb{1}, \quad D = \mathbb{1} + \epsilon_0 \Omega. \tag{5.9}$$

With this way of writing H and D, justified by the scaling law as dictated by evanescent waves, we infer that $[H, D] = 0$ and that the secular equation is equivalent to

$$\left| \frac{\Delta_0 \Omega + E_0}{1 + \epsilon_0 \Omega} - E \right| = 0, \tag{5.10}$$

where ϵ_0 is a small parameter and Δ_0 is a constant with units of energy. The above equation opens the door to the following possibility: we could manage to engineer Ω's spectrum in order to match a desired deformed energy spectrum E. We further explain this idea in the following section.

5.2 Spectral deformation with nearest-neighbor overlaps and on-site potential

From Eq. (5.10), an effective Hamiltonian is identified, H_{eff}, which is defined as

$$H_{\text{eff}} := \frac{\Delta_0 \Omega + E_0}{1 + \epsilon_0 \Omega}, \tag{5.11}$$

whose spectrum E is to be designed. Until now, Ω is unknown, but its deviations with respect to the orthogonal configuration can be estimated to first order in ϵ_0, i.e. for $\Omega = \Omega_0 + \epsilon_0 \delta\Omega$, and, by expanding H_{eff}, we have

$$|H_0 + \epsilon_0 (\Delta_0 \delta\Omega - H_0 \Omega_0) - E| = 0. \tag{5.12}$$

Given that E coincides with the spectrum of $H_0 = \Delta_0\Omega_0 + E_0$ (equispaced), we must look for a correction $\delta\Omega$ that compensates the deforming effect to first order in ϵ_0. Using the first order correction formula of perturbation theory, we conclude

$$\Delta_0 \langle \delta\Omega \rangle = \Delta_0 \langle \Omega_0^2 \rangle + E_0 \langle \Omega_0 \rangle = \frac{(E_n - E_0)^2}{\Delta_0} + \frac{E_0(E_n - E_0)}{\Delta_0}, \tag{5.13}$$

in the notation $|\rangle = |n\rangle$. For each n we have the result

$$\langle \delta\Omega \rangle_n = E_n(E_n - E_0)/\Delta_0^2, \tag{5.14}$$

for whatever spectrum E_n we wish to emulate. For linear spectra, $E_n = \alpha n + \beta$, we have

$$\langle \delta\Omega \rangle_n = \frac{\alpha^2 n^2}{\Delta_0^2} + \frac{2\alpha\beta - \alpha E_0}{\Delta_0^2} n + \frac{\beta^2}{\Delta_0^2} - \frac{\beta E_0}{\Delta_0^2}, \tag{5.15}$$

enforcing quadratic corrections in the geometrically designed operator Ω. Labeling $n = -j, \ldots, j$, according to the equispaced unperturbed problem, with solution $\Omega_0 = J_x \in \mathfrak{su}(2)$[1], helps to appreciate that

$$\operatorname{Tr}\Omega = \epsilon_0 \operatorname{Tr}\delta\Omega = (2j+1)\frac{(\beta^2 - \beta E_0)}{\Delta_0^2} + \frac{\alpha^2}{\Delta_0^2} \sum_{n=-j}^{j} n^2 \neq 0, \tag{5.16}$$

in general. This requires that $\delta\Omega$ contains diagonal elements whose sum does not vanish, discarding pure coupling deformations. The quadratic deformation is encoded by the matrix J_z^2 as the representation of the $\mathfrak{su}(2)$ algebra, while off-diagonal terms may come from J_x or J_y but we pick real matrices without loss of generality and write the general form

$$\delta\Omega = AJ_z^2 + BJ_x + C \tag{5.17}$$

where A, B and C are coefficients. We also have,

$$\begin{aligned} \langle x, n | J_z^2 | x, n \rangle &= \langle z, n | J_x^2 | z, n \rangle \\ &= \frac{1}{4} \left\langle J_+^2 + J_-^2 + 2(J^2 - J_z^2) \right\rangle_z \\ &= \frac{1}{2} \left[j(j+1) - n^2 \right], \end{aligned} \tag{5.18}$$

[1]The symbol $\mathfrak{su}(2)$ denotes the Lie algebra defined by the commutation relation $[J_l, J_m] = i\epsilon_{lmn}J_n$, where J_k, $k = 1, 2, 3$ are the components of the angular momentum operator. This commutation relation also defines the $\mathfrak{so}(3)$ algebra because the SU(2) group is locally isomorphic to the group of rotations in three dimensions, namely SO(3) [37]. Matrix elements are given by $\langle j', m' | J_\pm | j, m \rangle = \sqrt{(j \mp m)(j \pm m + 1)}\delta_{j'j}\delta_{m',m\pm1}$, and $\langle j', m' | J_3 | j, m \rangle = m\delta_{j',j}\delta_{m',m}$. The quantum number m can take values from $-j$ to j and $j \in \mathbb{N}/2$. Hence the tridiagonal J_x in our model.

since $\langle J_+^2 \rangle = \langle J_-^2 \rangle = 0$. Hence

$$\langle \delta\Omega \rangle_n = \frac{Aj(j+1)}{2} + C - \frac{An^2}{2} + Bn. \tag{5.19}$$

With the help of (5.15) we adjust the coefficients, obtaining

$$A = -\frac{2\alpha^2}{\Delta_0^2}, \quad B = \frac{2\alpha\beta - \alpha E_0}{\Delta_0^2}, \quad C = \frac{\beta(\beta - E_0)}{\Delta_0^2} + \frac{\alpha^2 j(j+1)}{\Delta_0^2} \tag{5.20}$$

such that we have the spectral rectifying perturbation

$$\delta\Omega \equiv -\frac{2\alpha^2}{\Delta_0^2} J_z^2 + \frac{\alpha(2\beta - E_0)}{\Delta_0^2} J_x + \frac{\beta(\beta - E_0)}{\Delta_0^2} + \frac{\alpha^2 j(j+1)}{\Delta_0^2}. \tag{5.21}$$

This expression is enough to achieve a spectrum $\alpha n + \beta$, but further simplifications are possible for our tight-binding systems if we recognize that $\epsilon_0 \to 0 \implies \alpha \to \Delta_0$ and $\beta \to E_0$, arriving at

$$\delta\Omega = -2J_z^2 + \frac{E_0}{\Delta_0} J_x + j(j+1), \tag{5.22}$$

which leads to the following expression for the Hamiltonian

$$H = E_0 + (\Delta_0 + \epsilon_0 E_0)\Omega_0 + \Delta_0 \epsilon_0 \left[j(j+1) - 2J_z^2 \right]. \tag{5.23}$$

The on-site potential, which used to be uniform, now controls the depth of the wells with a new prescription

$$V_{n_z} = E_0 + \Delta_0 \epsilon_0 \left[j(j+1) - 2n_z^2 \right], \tag{5.24}$$

which describes a faint parabolic profile around the baseline $E_0 = E$, see Fig. 5.1.

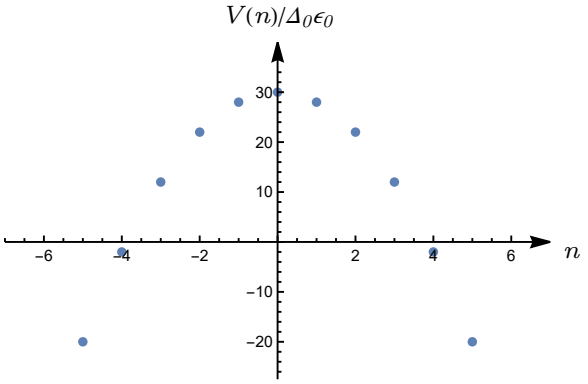

Figure 5.1: On-site potential deformation required for obtaining an equispaced energy spectrum for a compact configuration of potential wells. $E_0 = 0$ and $j = 5$.

Regarding the net effect of the deformation, we observe, as a side note, that the limit $D_{nn} = 1$ is correctly recovered to first order in ϵ_0 because corrections to Ω enter with ϵ_0 and the overall effect results in ϵ_0^2.

5.3 Spectral rigidity as a measure of equispaced spectra

Let us consider a set of N energy levels, in ascending order, $\{E_1, \ldots, E_N\}$, and denote it by Ξ. The spacing between successive elements of Ξ will be defined as $S_i = E_{i+1} - E_i$ with $i = 1, \ldots, N-1$. A perfectly equispaced set of energy levels is characterized for having all S_i equal to a constant. Such constant will then be equal to the mean energy spacing, $\bar{S} = \dfrac{\sum_{i=1}^{N-1} S_i}{N-1}$. In this ideal scenario, the normalized spacings, defined as $\tilde{S}_i := S_i/\bar{S}$, satisfy $\tilde{S}_i = 1$, for all i. So, we normalize the elements of the set $\{S_i\}_{i=1}^{N-1}$, by dividing by $\bar{S}$, to study the deviations from this case. Energies are also normalized with respect to E_0, obtaining the set $\tilde{E}_n = E_n/E_0$.

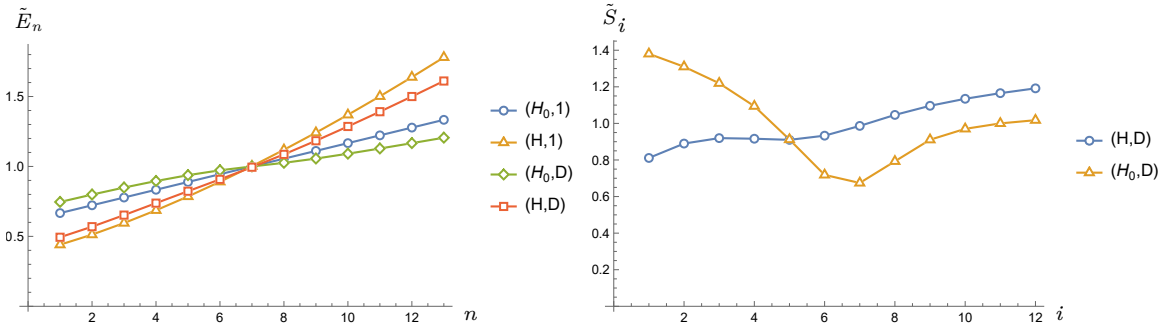

Figure 5.2: Normalized energy spectra (left panel) and spacings (right panel), for various models with $j = 6$, i.e. 13 sites, $\Delta_0 = 0.05$, and $E_0 = 0.9$. We chose $\epsilon_0 \approx 0.055$. In the first figure, the best result for an equispaced spectrum from non-orthogonal orbitals is shown in red, for the corrected Hamiltonian, H, and the addition of the metric operator, D. The rest of the models differ considerably from straight lines, except for $(H_0, 1)$, which, however, describes a dilute array. This is verified in the second panel, where the corrected model (blue circles) is closer to an equispaced spectrum than the original model (orange triangles). Perfectly equispaced spectra would be represented by a horizontal line.

Figs. 5.2 and 5.3 show the resulting sets of normalized energies and spacings for

both the fully-corrected Hamiltonian, Eq. (5.23), and a model that does consider the effect of non-orthogonal orbitals for describing a compact array of potential wells. The former is labeled by (H, D), and the latter by (H_0, D), where the $(,)$ notation is to be understood as the pair of operators that define the secular equation, $|H - ED| = 0$. Histograms of the respective data are presented in Figs. 5.4 and 5.5. There, it can be seen again that separations between consecutive energy values are distributed closer to 1 for the model with corrections than for uncorrected one. The other pairs of operators, namely $(H, 1)$ and $(H_0, 1)$, describe a dilute chain of potential wells with and without a deformed Hamiltonian.

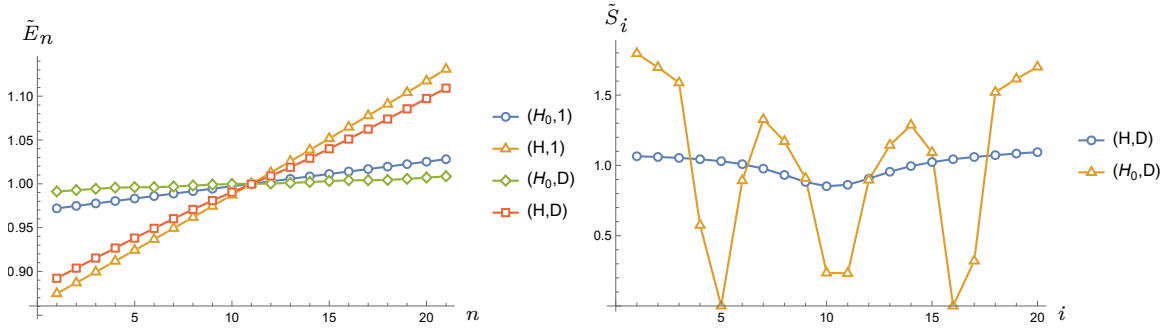

Figure 5.3: Normalized energy spectra (left) and spacings (right). In this case, $j = 10$, i.e. 21 sites, $\Delta_0 = 50$, $E_0 = 17840$ and $\epsilon_0 = 0.01$. In the second panel, the corrected model (blue circles) is closer to an equispaced spectrum than the original model (orange triangles).

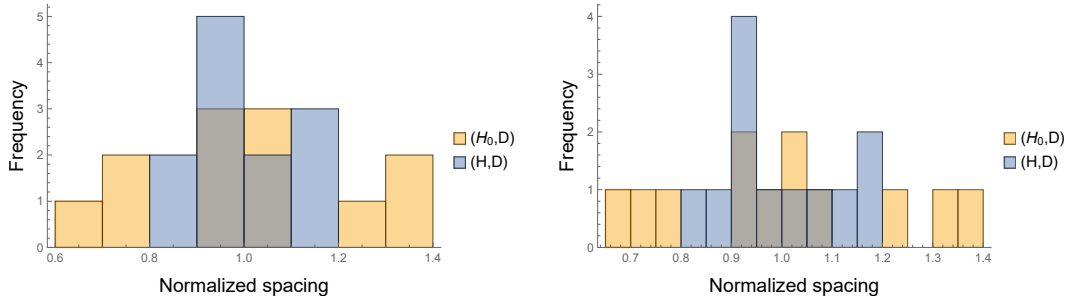

Figure 5.4: Histogram of energy spacings for a chain with $j = 6$. For the full non-orthogonal model (blue), the normalized energy spacings lie closer to 1 than for the tight-binding model without correction (orange). The different panels show an increasing number of bins, 9 and 15, showing clear trends and differences between blue and orange histograms. For the histogram at the left, $\sigma_{(H_0,D)} = 0.2136$ and $\sigma_{(H,D)} = 0.1130$

In order to measure energy equispacing, we introduce the spectral rigidity [39] as

$$\sigma = \sqrt{\sum_i p_i (E_i - \bar{E})^2}, \tag{5.25}$$

where $\bar{E} = \sum_i p_i E_i$ is the mean energy and $p_i = f_i / \sum_j f_j$ is the probability distribution extracted from bin frequency, f_i, as read from the histograms. The more equispaced the spectrum is, the smaller is the value of σ. This quantity was evaluated for the pairs (H_0, D) and (H, D), obtaining $\sigma_{(H_0,D)} = 0.2136$ and $\sigma_{(H,D)} = 0.1130$ for 15 bins, thus verifying that the corrected model is less spread than (H_0, D). This impressive result was obtained for a large value of $\epsilon = 0.055$. However, better results can be obtained for smaller values of the overlap, as shown in Fig. 5.3, where $\epsilon = 0.01$. In this case the spectral rigidity results in $\sigma_{(H_0,D)} = 0.5661$ and $\sigma_{(H,D)} = 0.0742$, for the same number of bins.

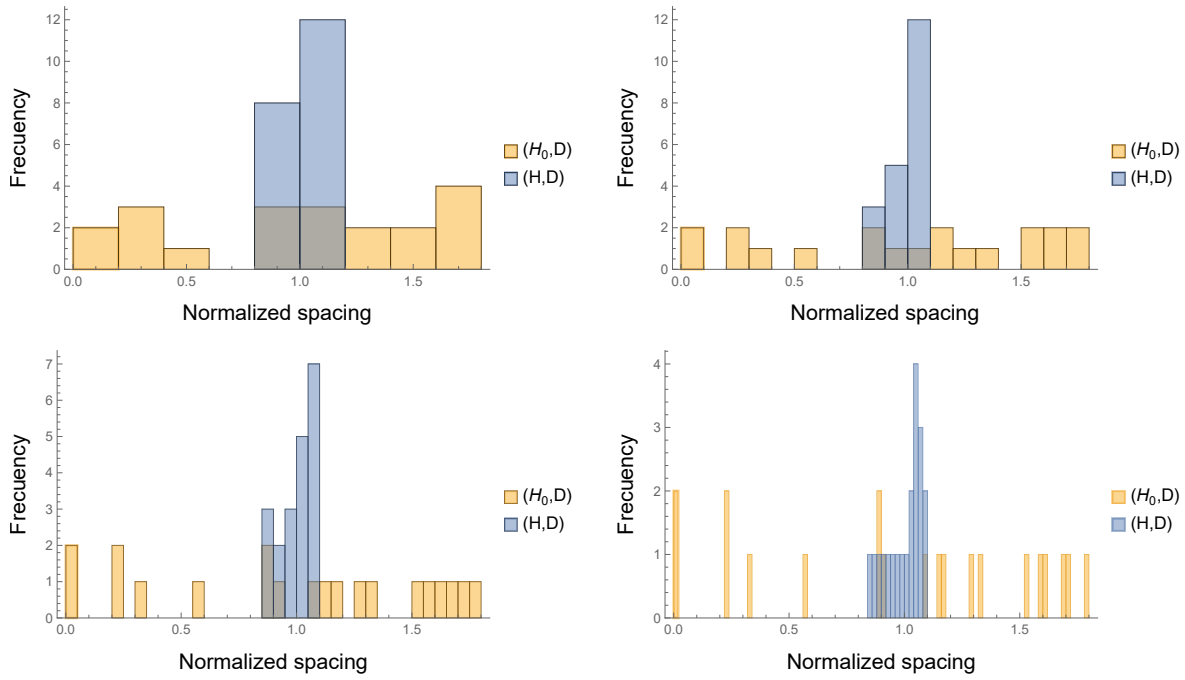

Figure 5.5: Histogram of energy spacings for a chain with 21 sites. A better coherence is expected for the evolution in the corrected model. The different panels show an increasing number of bins, 7, 13, 28, 57, with the corrected model (blue) having smaller spectral rigidity, $\sigma = 0.1, 0.074, 0.071, 0.074$, than a model for a finite oscillator without corrections (orange), $\sigma = 0.5495, 0.5661, 0.5739, 0.5774$. The listed values of σ are, respectively, for panels from left to right and top to bottom.

5.4 Coherent evolution: a realization of an electronic clock

In this section we present an example of an aperiodic configuration of potential wells that has the virtue of possessing a nearly equispaced spectrum. This system is depicted in Fig. 5.6. There, a configuration of three potential wells is shown with the ground state wavefunction superimposed.

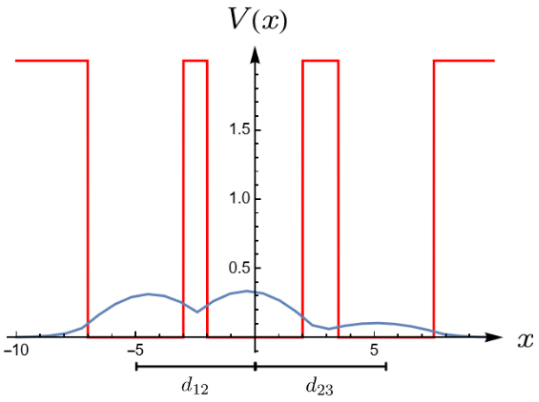

Figure 5.6: Deformed triple square well potential. This structure supports nearly equidistant energy levels. The width of each well is $L = 4$ cells. The ground state is shown in blue. The separation between wells, from left to right, as measured from their centers, is given by $d_{12} = 5$, $d_{23} = 5.5$ cells.

The equispaced sprectrum was computed by both diagonalizing the matrix Hamiltonian and by evaluating the resonance spectrum from the discrete Schrödinger equation, details of which are given in the next chapter. Both results coincide acceptably, as can be seen in Fig. 5.7, where the position of the transmission peaks agrees well with the lowest eigenvalues obtained from meshing the region that contains the system. In panel (b) of the same figure, the three lowest energy levels are shown to form a ladder with nearly evenly spaced steps. Then, a wavepacket was prepared inside this potential well structure as a superposition of the eigenfunctions of the problem. The wavepacket evolved coherently, as expected, for a few cycles, thus showing that an isochronous device can be engineered with potential wells of equal depth and width, but whose separations are changed from the periodic configuration, with an electronic wave packet moving in this structure constituting the oscillator. In Fig. 5.8, snapshots of the resulting coherent evolution are presented. We can see that after a certain period of time, τ, the wavepacket takes its original shape. In

the following section, we estimate the working frequency for a clock of this type.

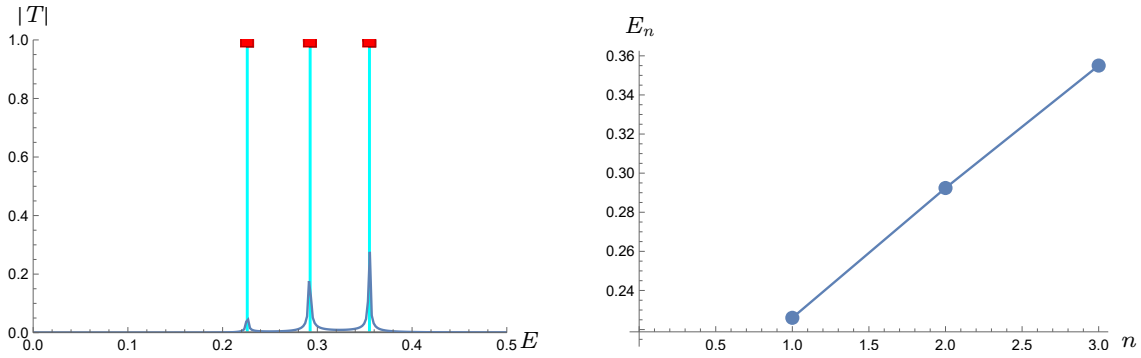

(a) (b)

Figure 5.7: Energy levels for the system shown in Fig. 5.6. $E = 0.2260, 0.2924, 0.3550$, in units where $V_0 = 2[8\hbar^2/mL^2]$. The level spacing for these levels results in 0.06639, 0.06262. The spectrum was verified by both meshing the spatial window that contains the system and by calculating the resonance spectrum. Transmission peaks coincide with the eigenvalues obtained from diagonalization. In the right panel energy levels are presented in a way so as to resemble a line with a constant slope.

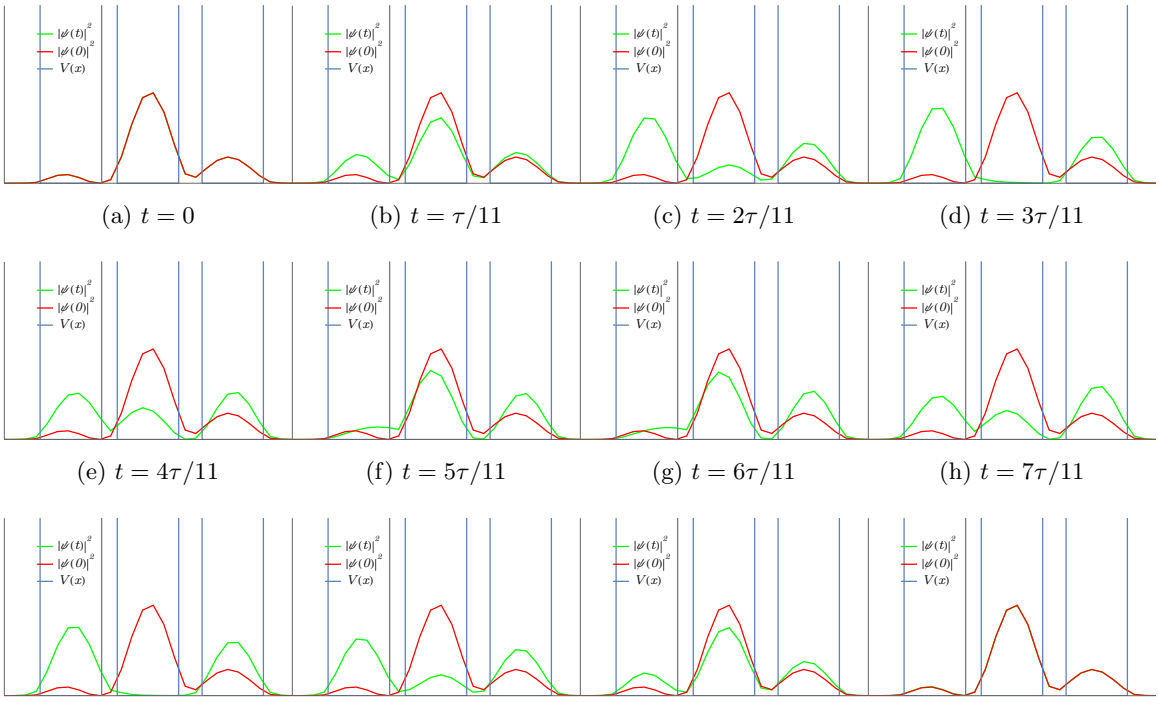

(a) $t = 0$ (b) $t = \tau/11$ (c) $t = 2\tau/11$ (d) $t = 3\tau/11$

(e) $t = 4\tau/11$ (f) $t = 5\tau/11$ (g) $t = 6\tau/11$ (h) $t = 7\tau/11$

(i) $t = 8\tau/11$ (j) $t = 9\tau/11$ (k) $t = 10\tau/11$ (l) $t = \tau$

Figure 5.8: Snapshots of coherent evolution. A wavepacket evolves in time (green profile) in an aperiodic structure that possess esquispaced energy levels. The evolution has a period of $\tau = 98$ for which the wavefunction at time t coincides with the initial wave packet (shown in red). The array of potential wells is shown in blue.

5.5 Discussion: electronic, atomic and quartz oscillations

In the following, the frequency for an electronic clock is estimated and the resulting value is compared against existing isochronous devices.

The most used clocks nowadays are those that owe its functioning to mechanical oscillations of a piezoelectric material, i.e. quartz clocks. The typical frequency of these oscillators is approximately equal to 30 kHz. Although electronic clocks would not be the most accurate in the world (the record being held by atomic clocks), the proposal of using an aperiodic nanostructure for designing a clock, working with electronic wave packets, has the potential of beating quartz in frequency, albeit it is more difficult to achieve this feat in accuracy. Among the common parts of a clock we have a power source, an oscillator, a controller, a counter and an indicator. To estimate the working frequency of an electronic oscillator, we need the mean level spacing of an aperiodic structure with an equispaced spectrum. For the system shown in Fig. 5.6, we got $\overline{\Delta E} = 0.0645$. Then, we can write the frequency as

$$\omega = \frac{\overline{\Delta E}}{\hbar}. \tag{5.26}$$

Using values such as $m = 9.109 \times 10^{-31}$ kg, for the mass of the electron, $\hbar = 1.054 \times 10^{-34}$ Js, and $L = 100$ nm, for a typical potential well width in the nanometer scale, see Ref. [32], we find that the mean energy spacing, in units of $8\hbar^2/mL^2 \approx 8 * 1.219 \times 10^{-24} \approx 9.757 \times 10^{-24}$ J, has the value of $\overline{\Delta E} \approx 6.293 \times 10^{-25}$ J, resulting in a working frequency $\omega \approx 5,970,622,461.302$ rad/s. The frequency, f, is obtained by dividing the angular frequency ω by 2π as reported in tables, so the result is one order of magnitude less than the working frequency of atomic clocks, and four orders of magnitude above quartz oscillations, making it a promising candidate for the replacement of current quartz technology. It is important to mention that this crude example can be significantly improved by looking for a more compact system of potential wells with more energy levels and with lower spectral rigidity. We know that this is possible and that the array of potential wells with these characteristics is not unique, in the sense that there are many solutions to the inverse problem [27]. However, this task lies outside the scope of this work. This isochronous device is compared with other oscillators in Table 5.1.

Table 5.1: Clocks comparison. Typical working frequency and accuracy for some isochronous devices.

Clocks			
Name	Oscillator	Frequency (Hz)	Accuracy
Pendulum	Hanging mass	2.006 Hz for a length of 1 m	Half a second a day, 1 part in 150,000
Quartz	Piezoelectric	32,768 Hz	±20 seconds/month, 20 parts in 2.592e+6
Atomic (Cs-133)	Electrons	9,192,631,770 Hz	1/15,000,000,000 of a second per year
Electronic (this work)	Electrons	$950,254,078$ Hz, better than Bloch oscillations with mean life 10^{-12} s, and less than 10 cycles [33].	$\sigma/N \approx 0.074/21$ $= 0.0035$ $\sim$ 1 part in 284, as achieved in this section

Now the results of this section are summarized, we introduced a generalized eigenvalue equation for the energy spectrum of a tight-binding system with overlapping localized atomic states. This problem originates from the findings reported in [17] where the spectrum of a finite oscillator was found to be deformed when studying arrays with small potential well interdistances. Then, it was noted that both the TB Hamiltonian and the overlap matrix can be written in terms of a tridiagonal operator, called Ω, because couplings and overlaps have a the same functional dependence. In the particular case of a finite oscillator model in the compact regime, this observation enabled the design of Ω such that the spectrum of the Hamiltonian for this system possesses an equispaced energy spectrum. It was found that a faint parabolic profile is needed, when studying the regime of small overlaps. It was verified that, when calculating the energy eigenvalues of tight-binding hamiltonians, with and without correction, the initially deformed spectrum was indeed rectified by the perturbation potential. The spectral rigidity, helped to quantify the degree of energy equispacing, and was evaluated for a few examples, both dense and dilute, founding acceptably small values. Then, an example of aperiodic structure, without on-site potential deformations, that

has evenly spaced energy levels was studied. Energy eigenvalues were obtained both with diagonalization and a scattering approach, finding good agreement. The periodic evolution of a wavepacket was presented. And, at the end of this chapter, the working frequency of an all-electronic clock was estimated, finding it of the order of magnitude of atomic clocks. This surpasses quartz mechanical oscillations. The additional chapter comprises the transport properties for these arrays. Reflection and transmission properties should exhibit the engineered spectrum of geometrically designed chains of resonators.

Chapter 6

Scattering in a shifted potential: exploring the metamaterial's resonance structure

In this chapter, it is shown how to calculate transport properties such as transmission and reflection coefficients from the discrete Schrödinger equation for engineered potential-well configurations, characterized for possessing an approximate equispaced spectrum. The procedure to achieve this task is implemented in a numerical routine, which can be found in Appendix C, and the resonance spectrum is then evaluated for both compact and dilute arrays.

6.1 Transport in an aperiodic and compact chain

In the following, it is described how to obtain the resonance spectrum of an arbitrary apodized potential using central discretization. We show how to propagate wavefunctions along the chain without smooth matching across regions, given their boundary conditions at one end of the array. In order to solve for the wavefunction at every point of the spatial window, we implement the method of continued fractions within the region of interest, from which transmission and reflection coefficients can be retrieved.

6.1.1 Discrete Schrödinger equation and change of reference of the potential

In a real experiment with open systems, only scattering states can be prepared. Thus, to discern the resonance structure of a system in a setting of this kind, it is necessary to shift (*to lift*) the zero-point of the potential. This amounts to a change of the reference energy such that $V_{\min} = 0$ and forcing the transmission channel to start at $E = 0$, in the region where there is no potential. Evidently, we also need to open the system. This is better explained if we consider, for instance, a harmonic oscillator potential. To explore the bound states for this problem, one has to cut the potential to a certain height making it look like a parabolic half pipe in a skating park. Outside of the parabolic trap, the potential is set to zero, such that impinging plane waves can be prepared. In this way the resonance spectrum of the half-pipe corresponds, approximately, to the bound states of the oscillator if it were closed. This principle works also for a chain of potential wells. However, our interest is to find a configuration of potential wells for a given resonance spectrum, which can be proved by preparing and propagating a scattering state through the system. This is done numerically in this work, evaluating R and T, as described in the following lines.

We start by writing the continuous Schrödinger equation

$$-\frac{d^2\psi}{dx^2} + V(x)\psi = E\psi, \tag{6.1}$$

as a discrete system, e.g. by central discretization of the Laplacian. The discretization is endowed with a length scale, given by the lattice parameter, a, say

$$-\frac{\psi_{n+1} - 2\psi_n + \psi_{n-1}}{a^2} + V_n\psi_n = E\psi_n. \tag{6.2}$$

The smaller a, the better. The approximation produces artificial spectral bands which resemble the true spectrum of the system in their lower parts. Since the potential can have any shape other than square barriers, it is better to employ the discrete Schrödinger equation, instead of the usual successive matching of boundary conditions (as we would normally do for Kronig-Penney model, but not this time). So, using the Eq. (6.2) as a recurrence in the site index, we can generate the wave at successive points if we start from a known region, namely, the asymptotic region. For example, knowing ψ_1 and ψ_2 allows to infer ψ_3, and so on. We need to specify V_n and E, where E is now a parameter. So, the algorithm shall take a specific value of E, propagate the wave, and give back the solution, ψ.

6.1.2 A formula for transmission and reflection coefficients

Once we have our potential in a localized region of space, and $V \geq 0$ everywhere, we must prepare a state in the asymptotic region, i.e. appropiate boundary conditions. Since there is no potential there, it is reasonable to fix ψ as a plane wave on the right hand side of the spatial window. For instance,

$$\psi_n = Te^{ikn} \tag{6.3}$$

On the left hand side we need a combination

$$\psi_n = e^{ikn} + Re^{-ikn}, \tag{6.4}$$

i.e. an incoming wave and a reflected wave, here both R and T can be complex. It is important to recall that the reflection and transmission are, respectively, $|R|^2$ and $|T|^2$.

Then, we shall make use of the discretized Schrödinger equation in order to obtain R and T, we have

$$-\Delta(\psi_{n+1} + \psi_{n-1} - 2\psi_n) + V_n\psi_n = E\psi_n \tag{6.5}$$

where $\Delta = \hbar^2/2ma^2$, a being the lattice parameter. Then we rewrite the previous equation as

$$\psi_{n-1} = \left[2 + a^2(V_n - E)\right]\psi_n - \psi_{n+1}, \tag{6.6}$$

i.e., ψ_{n-1} in terms of the successive values of the wavefunction. Defining

$$C_n := 2 + a^2(V_n - E), \tag{6.7}$$

we divide Eq. (6.6) by ψ_n such that the problem is now expressed in terms of the ratios of contiguous values of ψ along the chain. By choosing the simplest mesh, consisting of $N - N_0 + 1$ evenly spaced points, defined by the interval from N_0 to N, such that it contains the part of the potential that is of interest, and by propagating the values of the wavefunction in the asymptotic region, ψ_N and ψ_{N-1}, backwards in space, we end up with the following continued fraction

$$\frac{\psi_1}{\psi_2} = C_2 + \cfrac{1}{C_3 + \cfrac{1}{\ddots \cfrac{1}{C_{N-2} + \cfrac{1}{C_{N-1} + \cfrac{\psi_N}{\psi_{N-1}}}}}}. \tag{6.8}$$

If we wish to know the full solution, then, we must take the product of all the partial continued fractions or partial ratios that result relevant for the point of consideration. To write this succinctly, we introduce the definition

$$A_{n+1} := \frac{\psi_n}{\psi_{n+1}} \tag{6.9}$$

then

$$\psi_n = \prod_{n+1}^{N} A_n \psi_N. \tag{6.10}$$

for $n \in \{N_0, \ldots, N-2\}$. Additionally, if we consider the asymptotic region at the left of the potential, and propose the wavefunction there as $e^{ikn} + Re^{-ikn}$, we end up with the following relation

$$\frac{e^{ikN_0} + Re^{-ikN_0}}{e^{ikN_0+1} + Re^{-ikN_0+1}} = A_{N_0+1}(k), \tag{6.11}$$

that depends on the energy of the wave through k. Then we could get R as

$$R = \frac{e^{ik(N_0+1)}A_{N_0+1} - e^{ikN_0}}{e^{-ikN_0} - e^{-ik(N_0+1)}A_{N_0+1}} = e^{2i(kN_0+1)}\frac{A_{N_0+1} - e^{-ik}}{e^{ik} - A_{N_0+1}} \tag{6.12}$$

which allows to study the resonance spectrum of the system, with the reflection and transmission coefficients given above. By unitarity, $|T| = \sqrt{1 - |R|^2}$.

The set of values for T and R allows one to plot a curve as a function of E. The resulting curves should exhibit a peaked behavior. The values of E for which this happens are caused by complex resonances. But we are exploring the real line, we are constrained to such values of E. So, instead of the singularity in R and T we will see a finite peak whose location is close to the real part of the complex pole E. The imaginary part of the resonant E manifests as a width on the real line for E. Then we identify the set of peaks for all the real energies explored with the algorithm as the spectrum of the system. The idea is that if the system were closed (isolated from the outside) such peaks should become delta-type distributions.

6.2 Engineered lattices with an interstitial logarithmic law

In this section we briefly discuss the design of chains of potential wells with coupling laws corresponding to a finite oscillator in a dilute regime, the coupling law needed for the opposite case has been given in chapter 5.

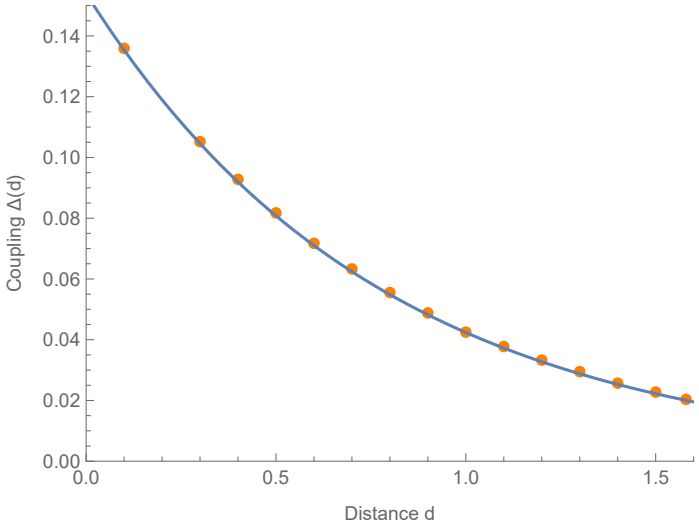

Figure 6.1: Approximate coupling law. The points were obtained by measuring the bandwidth, B, for a locally periodic system of 20 potential wells. The value of B allows to approximate the coupling as $\Delta = B/4$ at each point. Then, an exponential law was adjusted, $\Delta = \Delta_0 e^{-d/\lambda}$, for which $\Delta_0 = 0.154$ and $\lambda = 0.775$. All the points were obtained from a numerical resonance spectrum.

To have an idea of the values of couplings between sites for chains studied in the following, we first obtained a phenomenological coupling law, as plotted in Fig. 6.1. There, it is shown that couplings obey an exponentially decaying law. After doing this, we considered the previously mentioned coupling law, namely

$$\Delta(n) = \Delta_0 \sqrt{j(j+1) - n(n-1)} \tag{6.13}$$

then, by assuming an exponentially decaying function,

$$\Delta(d) = \Delta(0) e^{-d/\lambda} \tag{6.14}$$

we solve for d in terms of logarithms as

$$d_n = (-\lambda) \mathrm{Ln} \left[\frac{\Delta(n)}{\Delta(0)} \right]. \tag{6.15}$$

By employing the set of potential well interdistances generated by Eq. (6.15), and choosing $\Delta(0) = \Delta_0 \sqrt{j(j+1)}$, we obtain a set of spectra reported in the next section.

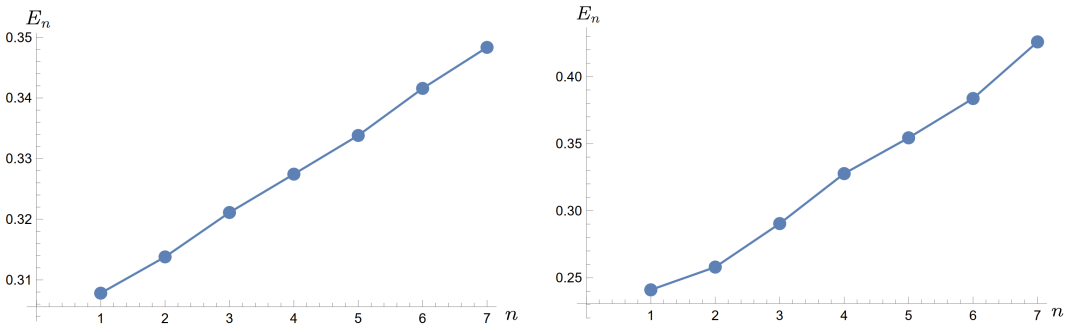

Figure 6.2: Energy levels for a finite oscillator. Dilute array, $\sigma_{\text{dilute}} = 0.0897$ (left), and a compact one, $\sigma_{\text{compact}} = 0.2629$ (right). The best equispaced spectrum is obtained for small overlaps, as in the left panel. The system of the right panel needs the correction by non-orthogonality of localized atomic states, Eq. (5.24).

6.3 Numerical resonance spectra

Figs. 6.2 and 6.3 show the numerical spectrum for systems of potential wells composed of 7 and 13 sites, respectively. We see from the first to the second figure, that the spectrum gets deformed for a compact array of lattice sites. We have calculated the spectral rigidity for both of these systems and have obtained the values, $\sigma_{\text{dilute}} = 0.0897$ and $\sigma_{\text{compact}} = 0.2629$. Thus we see the need of introducing corrections, as found in the previous chapter.

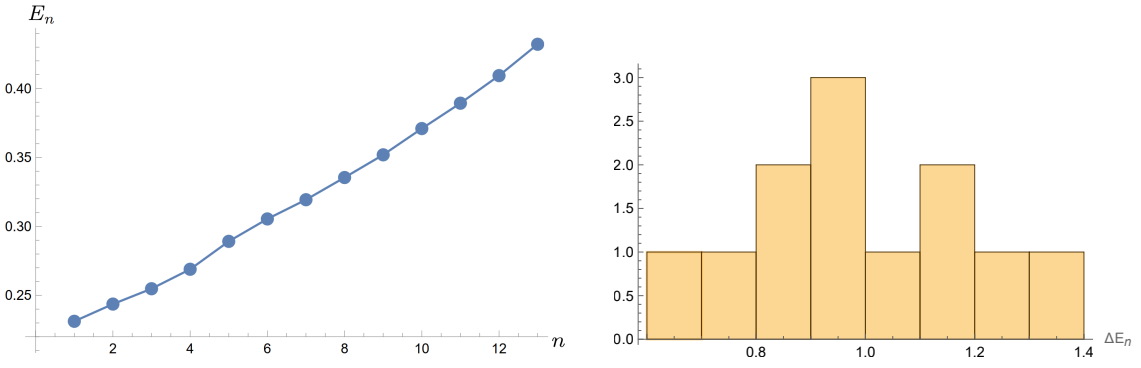

Figure 6.3: Almost-equispaced spectrum for a chain with $j = 6$, left panel. The histogram of energy spacings shows that they are distributed around 1. $\sigma = 0.1977$.

Lastly, we evaluate the set of resonances of the dilute version of the finite oscillator,

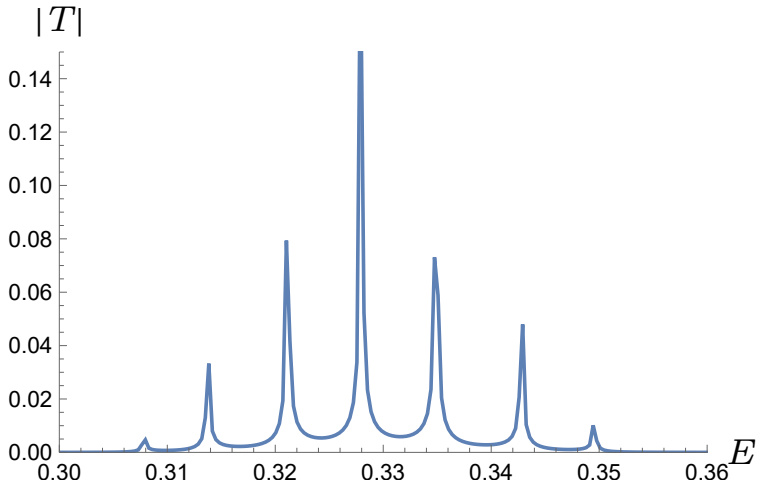

Figure 6.4: Resonance spectrum for a finite oscillator composed of 7 potential wells in the dilute regime. $\sigma = 0.1105$.

which possesses an equispaced spectrum. The result is presented in Fig. 6.4. The numerical resonance spectrum is an additional and original result in this work, and it is expected that it enables the scattering study of deformed arrays even with the corrections introduced. This will be explored in the future.

Chapter 7

Conclusions

By considering the overlap between isolated atomic states for compact configurations of potential wells, we have succeeded in emulating the asymmetric splitting of the energy levels of a dimer. The resulting theoretical spectrum, obtained from a tight-binding model in a non-orthogonal basis, was compared against available experimental data and the agreement was found to be good. To make the comparison, we first reviewed the inherent spectral asymmetry present in dimeric quantum systems. Then the problem of a tight-binding model for a pair of potential wells with overlapping localized states was posed and solved, finding the sought expressions for the energy levels which then were adjusted to experimental data with the help of an effective Schrödinger equation for electromagnetic waves in a cavity, which is based on the Helmholtz wave equation. This system represents a confirmation of the fact that deformations are only due to the non-orthogonality of atomic states since there are no further neighbors. In this way we achieved the first of our particular objectives presented in the introduction.

Regarding the second particular objective, we have the following comments. Infinite arrays of evenly spaced potential wells were also studied in connection with non-orthogonality of localized bases. We found that overlapping orbitals produce deformed energy bands in tight-binding representations. Evidently, the Kroning-Penney model produces similar results for chains of closely located sites; we focused on the third energy band, where asymmetries were more conspicuous. On the other hand, the tight-binding model without corrections was shown to fall short in reproducing similar results. Additionally, it was also shown that the energy spectrum of a periodic potential can be approximated with high accuracy by a tight-binding model with multiple neighbors or non-orthogonal orbitals.

In an exact manner, there exists a nearest neighbor tight-binding Hamiltonian that best approximates any energy band, as reviewed in chapter 3. This model can be written with the help of the Fourier transform of the energy spectrum, plus the Wannier transform for the wave functions.

Even though we can take localized states as Wannier functions (WFs) in the approximation of dilute resonators, we cannot do this when the overlap is significantly larger. In chapter 4, we calculated WFs by taking into account non-negligible overlaps between neighboring atomic states, thus accomplishing the third particular objective. In the case of a dimer, we found that WFs acquire a shape that looks similar to an isolated state except that its exponential tail oscillates to ensure orthogonality with its neighbor. On the other hand, WFs for translationally invariant potentials take contributions from both nearest neighbors, and can be calculated up to second order in the overlap parameter, which means that we can consider up to next-to-nearest contributions from further potential wells. A phase in the Wannier transform was shown to give rise to WFs of different shapes. This last part is related to the problem of maximally localized WFs.

Then, it was shown that the spectrum of a tight-binding Hamiltonian operator for a chain of potential wells with overlapping on-site wavefunctions can be designed with the help of a tridiagonal operator, called Ω in this work, thanks to the fact that both couplings and overlaps decay exponentially with potential well interdistances. A generalized eigenvalue equation was introduced, and by working perturbatively, for small overlaps, the necessary corrections to produce equispaced energy levels were found. The spectral rectification was verified and the spread of the energy level distribution around the equispaced case was quantified with the spectral rigidity, finding low acceptable values. The concept of an all-electronic clock was then introduced, finding a working frequency one order of magnitude smaller than atomic clock oscillations. The results of this section show that we have attain the fourth particular objective of finding aperiodic and compact configuration of potential wells with corrections from non-orthogonal orbitals.

Finally, as an additional result, the resonance spectrum of an aperiodic structure of potential wells was analyzed numerically. A method for calculating transport properties for an arbitrary shifted potential based on continued fractions was described. This method was implemented in a numerical routine and the spectrum of a dilute array of potential wells was evaluated, finding nearly equispaced energy eigenvalues. This study gives the hope that our results could be taken to a laboratory stage, in diverse emulations such as

dielectric disks, optical lattices, aluminum resonators, photonic crystals, phononic crystals, and the one that holds more promise, semiconductor nanostructures, where an electronic wavepacket is expected to evolve coherently, expecting to perform better than common clocks that work with quartz as a mechanical oscillator. The current mastery of techniques for growing materials would represent an advantage for mass production and might be useful for laboratories that want high accuracy at lower prices with respect to an atomic clock.

Appendix A

Even solutions for an infinite well with a delta obstacle

Here, it is shown that (2.7) is indeed a solution to the stationary schrödinger problem with potential given by (2.6). We start by recasting (2.7) in the more compact form

$$\psi(x) = 2\mathcal{N}\sinh[k(l/2 - |x|)], \tag{A.1}$$

where $\mathcal{N}$ is the corresponding normalization constant. The second derivative of $\psi(x)$ is

$$\frac{d^2\psi(x)}{dx^2} = 2\mathcal{N}\frac{d}{dx}\left\{\cosh[k(l/2 - |x|)] * (-k\,\mathrm{sgn}(x))\right\}, \tag{A.2}$$

where $\mathrm{sgn}(x)$ is the so-called sign function, defined by

$$\mathrm{sgn}(x) := \begin{cases} -1 & \text{if } x < 0, \\ 0 & \text{if } x = 0, \\ 1 & \text{if } x > 0. \end{cases} \tag{A.3}$$

Such function makes its appearance since $\frac{d|x|}{dx} = \mathrm{sgn}(x)$. By further noting that $\frac{d\,\mathrm{sgn}(x)}{dx} = 2\delta(x)$, we can write

$$\begin{aligned} \frac{d^2\psi(x)}{dx^2} &= -2k\mathcal{N}\{\sinh[k(l/2 - |x|)] * (-k\,\mathrm{sgn}(x)) \\ &* \quad \mathrm{sgn}(x) + \cosh[k(l/2 - |x|)] * 2\delta(x)\}. \end{aligned} \tag{A.4}$$

And, given that $\text{sgn}^2(x) = 1$, the previous expression is simplified to

$$\begin{aligned} \frac{d^2\psi(x)}{dx^2} &= -2k\mathcal{N}\{\sinh[k(l/2 - |x|)] * (-k) \\ &+ \cosh[k(l/2 - |x|)] * 2\delta(x)\}. \end{aligned} \tag{A.5}$$

In the right hand side of (A.5), we identify the expression for the wavefunction in the first term whereas the second term can be managed to give a term proportional to $\psi(x)$, for this, we remind the reader of the identity $f(x)\delta(x) = f(0)\delta(x)$ (under the integral operation). Thus we multiply and divide the second term by $\psi(0)/2 = \sinh(kl/2)$ so that (A.5) transforms to

$$\frac{d^2\psi(x)}{dx^2} = k^2\psi(x) - 2k\coth[kl/2]\psi(x)\delta(x). \tag{A.6}$$

This is the Schrödinger equation with an overall minus sign corresponding to potential (2.6) and $E = -k^2$. From this last equation we can read the transcendental condition for determining the allowed energy eigenvalues, namely

$$2k\coth(kl/2) = \gamma \tag{A.7}$$

which is another way of expressing the equation found in table 2.1.

Appendix B

Fourier transform of $\cos^k \theta$

The Fourier transform of $\cos^k \theta$ can be calculated as follows

$$\begin{aligned}
\int_{-\pi}^{\pi} d\theta e^{iq\theta} \cos^k \theta &= \int_{-\pi}^{\pi} d\theta e^{iq\theta} \left(\frac{e^{i\theta} + e^{-i\theta}}{2} \right)^k \\
&= \int_{-\pi}^{\pi} d\theta e^{iq\theta} \frac{e^{-ik\theta}}{2^k} \sum_{r=0}^{k} e^{2i\theta r} \binom{k}{r} \\
&= \sum_{r=0}^{k} \binom{k}{r} \frac{1}{2^k} \int_{-\pi}^{\pi} d\theta e^{i(q-k+2r)\theta}. \qquad \text{(B.1)}
\end{aligned}$$

The last integral is equal to $2\pi\delta_{q+2r,k}$. Hence, Eq. (4.17) follows.

Appendix C

Mathematica code for resonance spectra of 1D shifted potentials

```
(*Kronecker delta to define matrix elements*)
d[n_,m_]:=KroneckerDelta[n,m];
(*Pulse function to construct arrays of potential wells*)
Pulse[a_,b_,n_]:=If[-b/2+a<n&&n<a+b/2,1,0];

(*Fix the parameters for the discretization*)
numberofpoints=30;
x1=10;
windowlength=x1*2;
numberofintervals=numberofpoints-1;
lp=windowlength/numberofintervals;

(*Stipulate the potential function*)
V0=-2;
potential[x_]:=V0*Pulse[-5,4,x]+V0*Pulse[0,4,x]+V0*Pulse[5.5,4,x]-V0;

(*Define the coefficient given in Eq. (6.7) of this thesis*)
cc[n_,energy_]:=2+lp^2*(potential[n*lp-x1]-energy);

(*Establish the energy interval to be examined*)
maxenergy=0.5;
minenergy=0;
numberofenergies=250;
numberofintervalsofenergy=numberofenergies-1;
quantumofenergy=(maxenergy-minenergy)/numberofintervalsofenergy;

(*Prepare vectors for resonance data*)
```

```
reflectiondata=Table[{0,0},numberofenergies];
transmissiondata=Table[{0,0},numberofenergies];
ii=1;

(*Start sweeping energy values to look for transmission maxima*)
For[energy=minenergy,energy<=maxenergy,energy+=N[quantumofenergy],{

(*Set the asymptotic wave*)
wavefunction=ConstantArray[0,numberofpoints],
wavefunction[[numberofpoints]]=Cos[Sqrt[energy]*(numberofpoints-1)*lp]+
                               I*Sin[Sqrt[energy]*(numberofpoints-1)*lp];,
wavefunction[[numberofpoints-1]]=Cos[Sqrt[energy]*(numberofpoints-2)*lp]+
                                 I*Sin[Sqrt[energy]*(numberofpoints-2)*lp];,

(*Compute all the continued fractions needed*)
B=ConstantArray[0,numberofpoints-1];,
denominator=ConstantArray[0,numberofpoints-2];,

B[[numberofpoints-1]]=N[wavefunction[[(numberofpoints)]]/
                       wavefunction[[(numberofpoints-1)]]];,
For[kk=2,kk<=numberofpoints-1,kk++,{
denominator[[numberofpoints-kk]]=cc[numberofpoints-kk,energy]-
                                 B[[numberofpoints-kk+1]],
If[denominator[[numberofpoints-kk]]!=0,
        B[[numberofpoints-kk]]=1/denominator[[numberofpoints-kk]],
              Print["El denominador es cero"]]}],

A=ConstantArray[0,numberofpoints-1];,

For[kk=1,kk<=numberofpoints-1,kk++,A[[kk]]=1/B[[kk]]];,

(*Obtain the wavefunction at any lattice point from A coefficients*)
For[kk=1,kk<=numberofpoints-1,kk++,
wavefunction[[numberofpoints-kk]]=N[Product[A[[numberofpoints-i]],{i,1,kk}]*
                                   wavefunction[[numberofpoints]]]];,

(*Evaluate the reflection amplitude*)
reflectionamplitude=N[(Exp[I*Sqrt[energy]*lp]*A[[1]]-1)/
                     (1-Exp[-I*Sqrt[energy]*lp]*A[[1]])];,
reflection=N[Abs[reflectionamplitude]];,


(*Collect reflection and transmission data*)
reflectiondata[[ii]][[1]]=energy;,
```

```
reflectiondata[[ii]][[2]]=reflection;,
transmissiondata[[ii]][[1]]=energy;,
transmissiondata[[ii]][[2]]=Sqrt[1-reflection^2];,
ii=ii+1}];

(*Show the resulting resonance spectrum*)
Print[{ListPlot[reflectiondata,PlotRange->{{minenergy,maxenergy},{0,1}},
AxesLabel->{Style["E",15,Italic,Black,FontFamily->"Latin Modern Roman 7"],
Style["|R|",15,Italic,Black,FontFamily->"Latin Modern Roman 7"]},
ImageSize->Medium],
ListPlot[transmissiondata,Joined->True,PlotRange->{{minenergy,maxenergy},{0,1}},
AxesLabel->{Style["E",15,Italic,Black,FontFamily->"Latin Modern Roman 7"],
Style["|T|",15,Italic,Black,FontFamily->"Latin Modern Roman 7"]},
ImageSize->Medium]}];
```

Bibliography

[1] Gorishnyy, T., Maldovan, M., Ullal, C., & Thomas, E. (2005). Sound ideas. *Physics World*, 18(12), 24.

[2] Pendry, J. B., Holden, A. J., Robbins, D. J., & Stewart, W. J. (1999). Magnetism from conductors and enhanced nonlinear phenomena. *IEEE Transactions on Microwave Theory and Techniques*, 47(11), 2075-2084.

[3] Veselago, V. G. (1968). THE ELECTRODYNAMICS OF SUBSTANCES WITH SIMULTANEOUSLY NEGATIVE VALUES OF ϵ AND μ. *Soviet Physics Uspekhi*, 92(7), 517.

[4] Franco-Villafañe, J. A., Sadurni, E., Barkhofen, S., Kuhl, U., Mortessagne, F., & Seligman, T. H. (2013). First experimental realization of the Dirac oscillator. *Physical Review Letters*, 111(17), 170405.

[5] Sadurni, E. (2008). Klein–Gordon and Dirac gyroscopes. *Journal of Physics A: Mathematical and Theoretical*, 42(1), 015209.

[6] Sadurni, E., Franco-Villafañe, J. A., Kuhl, U., Mortessagne, F., & Seligman, T. H. (2013). Schematic baryon models, their tight binding description and their microwave realization. *New Journal of Physics*, 15(12), 123014.

[7] Gomes, K. K., Mar, W., Ko, W., Guinea, F., & Manoharan, H. C. (2012). Designer Dirac fermions and topological phases in molecular graphene. *Nature*, 483(7389), 306-310.

[8] Geim, A. K., & Novoselov, K. S. (2007). The rise of graphene. *Nature Materials*, 6(3), 183-191.

[9] Reich, E. S. (2013). Graphene knock-offs probe ultrafast electronics. *Nature*, 497(7450), 422-423.

[10] Semenoff, G. W. (1984). Condensed-matter simulation of a three-dimensional anomaly. *Physical Review Letters*, 53(26), 2449.

[11] Tarruell, L., Greif, D., Uehlinger, T., Jotzu, G., & Esslinger, T. (2012). Creating, moving and merging Dirac points with a Fermi gas in a tunable honeycomb lattice. *Nature*, 483(7389), 302-305.

[12] Barkhofen, S., Bellec, M., Kuhl, U., & Mortessagne, F. (2013). Disordered graphene and boron nitride in a microwave tight-binding analog. *Physical Review B*, 87(3), 035101.

[13] Bellec, M., Kuhl, U., Montambaux, G., & Mortessagne, F. (2013). Tight-binding couplings in microwave artificial graphene. *Physical Review B*, 88(11), 115437.

[14] Bellec, M., Kuhl, U., Montambaux, G., & Mortessagne, F. (2013). Topological transition of Dirac points in a microwave experiment. *Physical Review Letters*, 110(3), 033902.

[15] Kuhl, U., Barkhofen, S., Tudorovskiy, T., Stöckmann, H. J., Hossain, T., De Parny, L. D. F., & Mortessagne, F. (2010). Dirac point and edge states in a microwave realization of tight-binding graphene-like structures. *Physical Review B*, 82(9), 094308.

[16] Peleg, O., Bartal, G., Freedman, B., Manela, O., Segev, M., & Christodoulides, D. N. (2007). Conical diffraction and gap solitons in honeycomb photonic lattices. *Physical Review Letters*, 98(10), 103901.

[17] Rivera-Mociños, E., & Sadurní, E. (2016). Inverse lattice design and its application to bent waveguides. *Journal of Physics A: Mathematical and Theoretical*, 49(17), 175302.

[18] Sadurni, E. (2011). The Dirac-Moshinsky oscillator: theory and applications. *AIP Conference Proceedings.* 1334(1) 249-290

[19] Wu, L. H., & Hu, X. (2016). Topological properties of electrons in honeycomb lattice with detuned hopping energy. *Scientific Reports*, 6(1), 24347.

[20] Zandbergen, S. R., & de Dood, M. J. (2010). Experimental observation of strong edge effects on the pseudodiffusive transport of light in photonic graphene. *Physical Review Letters*, 104(4), 043903.

[21] Bittner, S., Dietz, B., Miski-Oglu, M., & Richter, A. (2012). Extremal transmission through a microwave photonic crystal and the observation of edge states in a rectangular Dirac billiard. *Physical Review B*, 85(6), 064301.

[22] Dreisow, F., Keil, R., Tünnermann, A., Nolte, S., Longhi, S., & Szameit, A. (2012). Klein tunneling of light in waveguide superlattices. *Europhysics Letters*, 97(1), 10008.

[23] Nualpijit, P., Sinner, A., & Ziegler, K. (2018). Tunable transmittance in anisotropic two-dimensional materials. *Physical Review B*, 97(23), 235411.

[24] Bellec, M., Kuhl, U., Montambaux, G., & Mortessagne, F. (2014). Manipulation of edge states in microwave artificial graphene. *New Journal of Physics*, 16(11), 113023.

[25] Bittner, S., Dietz, B., Miski-Oglu, M., Iriarte, P. O., Richter, A., & Schäfer, F. (2010). Observation of a Dirac point in microwave experiments with a photonic crystal modeling graphene. *Physical Review B*, 82(1), 014301.

[26] Sadurni, E., Seligman, T. H., & Mortessagne, F. (2010). Playing relativistic billiards beyond graphene. *New Journal of Physics*, 12(5), 053014.

[27] Rivera Mociños, E. (2017). *Propagación y transporte en guías de ondas desordenadas con esquinas.* [Doctoral thesis, Benemérita Universidad Autónoma de Puebla].

[28] Kronig, R. De L., & Penney, W. G. (1931). Quantum mechanics of electrons in crystal lattices. *Proceedings of the Royal Society A: Mathematical, Physical and Engineering Sciences*, 130(814), 499-513.

[29] Stöckmann, H.-J. (1999). *Quantum chaos: An introduction.* Cambridge University Press.

[30] Sadurní, E. (2014). Transparent lattices and their solitary waves. *Physical Review E*, 90(3), 033205.

[31] Sadurni, E. (2013). Time-dependent Stark ladders: exact propagator and caustic control. *Journal of Physics A: Mathematical and Theoretical*, 46(13), 135302.

[32] Wang, R. L., Zhang, J., & Hu, Q. F. (2008). Simulation of band gap structures of 1D photonic crystal. *Journal of the Korean Physical Society*, 52(1), 71-74.

[33] Waschke, C., Roskos, H. G., Schwedler, R., Leo, K., Kurz, H., & Köhler, K. (1993). Coherent submillimeter-wave emission from Bloch oscillations in a semiconductor superlattice. *Physical Review Letters*, 70(21), 3319.

[34] Mitchell, G. E., Richter, A., & Weidenmüller, H. A. (2010). Random matrices and chaos in nuclear physics: Nuclear reactions. *Reviews of Modern Physics*, 82(4), 2845-2901

[35] Kittel, C. (2005). *Introduction to solid state physics* (8th ed.). John Wiley & Sons, Inc.

[36] Marzari, N., Mostofi, A. A., Yates, J. R., Souza, I., & Vanderbilt, D. (2012). Maximally localized Wannier functions: Theory and applications. *Reviews of Modern Physics*, 84(4), 1419.

[37] Greiner, W., & Müller, B. (1994). *Quantum mechanics: Symmetries* (2nd ed.). Springer Berlin, Heidelberg.

[38] Watson, G. N. (1995). *A treatise on the theory of Bessel functions* (2nd ed., Cambridge Mathematical Library ed.). Cambridge University Press.

[39] Ott, E. (1993). *Chaos in dynamical systems*. Cambridge University Press.

Oficio No. IF-SACAD175/2023

Asunto: Carta Aval

MTRO. ALFREDO AVENDAÑO ARENAZA
DIRECTOR GENERAL DE BIBLIOTECAS
BENEMÉRITA UNIVERSIDAD AUTÓNOMA DE PUEBLA
PRESENTE

El que suscribe, Director del Instituto de Física "Ing. Luis Rivera Terrazas" de la Benemérita Universidad Autónoma de Puebla, **AVALA** con base en los archivos que se encuentran en este Instituto que la tesis de **JOSE GUADALUPE SANTIAGO GARCIA**, matrícula: **221470428**, cuyo título es: **"SPECTRAL DESIGN OF METAMATERIALS WITH NON-ORTHOGONAL ORBITALS"**, ha sido *revisada* y *aprobada* por el Comité respectivo para presentar su examen de grado de **MAESTRÍA EN CIENCIAS (FÍSICA)** el próximo día **18 de octubre de 2023** a las **15:00** horas en el auditorio del IFUAP. Dicho Comité está integrado por los siguientes profesores:

Dr. Eduardo Jonathan Torres Herrera	**Presidente**
Dr. Nykolay Makarov	**Secretario**
Dra. Carolina Janani Diliegros Godines	**Vocal**
Dr. Emerson Leao Sadurní Hernández	**Vocal**

Se informa también que dicha tesis se encuentra lista para su impresión.

Sin otro asunto que el particular, reciba mi más alto reconocimiento.

A T E N T A M E N T E
"Pensar Bien, Para Vivir Mejor"
Puebla, Pue., a 28 de septiembre de 2023

DR. FELIPE PÉREZ RODRÍGUEZ
DIRECTOR

DR*FPR/DRA*MECR/LAE*mhr

Instituto de Física
"Luis RiveraTerrazas"
Av. San Claudio esq. 18 Sur, Edif. IF1,
Ciudad Universitaria, Col. San Manuel
Puebla, Pue. C.P. 72570
01 (222) 229 55 00 Ext. 5610, 5611, 2008